

A puzzle solved after two decades: SN 2002gh among the brightest of superluminous supernovae

Régis Cartier,^{1*} Mario Hamuy,^{2,3} Carlos Contreras,⁴ Joseph P. Anderson,⁵
 Mark M. Phillips,⁴ Nidia Morrell,⁴ Maximilian D. Stritzinger,⁶ Emilio D. Hueichapan,¹
 Alejandro Clocchiatti,^{7,8} Miguel Roth,⁴ Joanna Thomas-Osip,⁹ and Luis E. González¹⁰

¹*Cerro Tololo Inter-American Observatory, NSF's National Optical-Infrared Astronomy Research Laboratory, Casilla 603, La Serena, Chile*

²*VicePresident and Head of Mission of AURA-O in Chile, Avda. Presidente Riesco 5335 Suite 507, Santiago, Chile*

³*Hagler Institute for Advanced Studies, Texas A&M University, Texas, USA*

⁴*Las Campanas Observatory, Carnegie Observatories, Casilla 601, La Serena, Chile*

⁵*European Southern Observatory, Alonso de Córdova 3107, Casilla 19, Santiago, Chile*

⁶*Department of Physics and Astronomy, Aarhus University, Ny Munkegade 120, 8000 Aarhus C, Denmark*

⁷*Instituto de Astrofísica, Facultad de Física, Pontificia Universidad Católica de Chile, Av. Vicuña Mackenna 4860, Santiago, Chile*

⁸*Millennium Institute of Astrophysics, Nuncio Monseñor Sótero Sanz 100, Providencia, Santiago, Chile*

⁹*Gemini Observatory, NSF's National Optical-Infrared Astronomy Research Laboratory, Casilla 603, La Serena, Chile*

¹⁰*Departamento de Astronomía, Universidad de Chile, Casilla 36-D, Santiago, Chile*

24 August 2021

ABSTRACT

We present optical photometry and spectroscopy of the superluminous SN 2002gh from maximum light to +202 days, obtained as part of the Carnegie Type II Supernova (CATS) project. SN 2002gh is among the most luminous discovered supernovae ever, yet it remained unnoticed for nearly two decades. Using Dark Energy Camera archival images we identify the potential SN host galaxy as a faint dwarf galaxy, presumably having low metallicity, and in an apparent merging process with other nearby dwarf galaxies. We show that SN 2002gh is among the brightest hydrogen-poor SLSNe with $M_V = -22.40 \pm 0.02$, with an estimated peak bolometric luminosity of $2.6 \pm 0.2 \times 10^{44}$ erg s⁻¹. We discount the decay of radioactive nickel as the main SN power mechanism, and assuming that the SN is powered by the spin down of a magnetar we obtain two alternative solutions. The first case, is characterized by significant magnetar power leakage, and M_{ej} between 0.8 and 1.6 M_{\odot} , $P_{\text{spin}} = 3.4$ ms, and $B = 5 \times 10^{13}$ G. The second case does not require power leakage, resulting in a huge ejecta mass of about 30 M_{\odot} , a fast spin period of $P_{\text{spin}} \sim 1$ ms, and $B \sim 1.6 \times 10^{14}$ G. We estimate a zero-age main-sequence mass between 16 and 19 M_{\odot} for the first case and of about 135 M_{\odot} for the second case. The latter case would place the SN progenitor among the most massive stars observed to explode as a SN.

Key words: supernovae: general — supernovae: individual (SN 2002gh)

1 INTRODUCTION

The first half of the 21st century will be remembered as a revolutionary epoch for time-domain astronomy. Thanks to large area and untar-geted transient surveys, astronomers are exploring the time-domain Universe to an unprecedented level, discovering transient events that span a wide range of timescales and luminosities. One of the most spectacular such transients are the rare class of supernovae (SNe) characterized by their extremely bright peak luminosities (≈ -21 mag at optical wavelengths) powered by a non-standard source of energy, that have challenged our understanding of massive star evolution and explosion.

These rare and bright SNe are commonly referred to as superluminous SNe (SLSNe). Like their lower luminosity cousins they are

divided into subtypes based on the presence of hydrogen in their spectra as hydrogen-rich (Type II) and hydrogen-poor (Type I) (see [Moriya et al. 2018](#); [Gal-Yam 2019a](#)). Some SLSNe-II show relatively narrow hydrogen emission lines on top of a broad component, characteristic of SNe Type IIn (see [Schlegel 1990](#)), and evidence of interaction between the energetic SN ejecta and a massive hydrogen-rich circum-stellar medium, such as SN 2006gy ([Smith et al. 2007](#); [Ofek et al. 2007](#)). These SLSNe-II are usually considered the bright end of Type IIn SNe, although it is unclear whether an additional power source other than the strong ejecta-CSM interaction and radioactive decay significantly contributes to their extreme luminosities (see e.g., [Woosley et al. 2007](#); [Jerkstrand et al. 2020](#)). The idea of an additional power source is reinforced by some SLSNe-II that do not show clear signatures of strong ejecta-CSM interaction ([Gezari et al. 2009](#); [Miller et al. 2009](#); [Inserra et al. 2018](#); [Dessart 2018](#)). A potential power source is the energy injection from the spin down

* regis.cartier@noirlab.edu

of a fast rotating neutron star with an extremely powerful magnetic field, a magnetar, as explained below. Other notable events of the SLSN class, are a handful of objects initially classified as hydrogen-poor SLSNe, but several days after maximum light reveal hydrogen features and signatures of ejecta-CSM interaction (Yan et al. 2015, 2017), suggesting that some hydrogen-poor SLSNe lose their hydrogen envelopes shortly before their final explosion.

Objects such as SN 1999as (Knop et al. 1999), SN 2005ap (Quimby et al. 2007), SCP 06F6 (Barbary et al. 2009), and SN 2007bi (Gal-Yam et al. 2009) were the first SLSN-I reported, several years before they were distinguished as a separate SN class. Their bright peak luminosities together with the identification of a common set of spectral features made it possible to distinguish them as members of a completely new SN class (Quimby et al. 2011). These SLSNe are characterized by their extreme peak luminosities, very blue and nearly featureless optical spectral emission, the lack of hydrogen and helium lines and the presence of O II and C II absorption lines before and close to maximum light (Quimby et al. 2011). A few weeks after maximum light, when the ejecta are cool enough, SLSN-I spectra become similar to SNe Ic (e.g., Pastorello et al. 2010) or to broad line SNe Ic (SNe Ic-BL; Liu et al. 2017) at an early phase. Their nebular spectra also show some similarity with the nebular spectra of SNe Ic-BL (Milisavljevic et al. 2013; Jerkstrand et al. 2017; Nicholl et al. 2016b, 2019).

One of the first models proposed to account for the large luminosity displayed by SLSNe was the radioactive decay of several solar masses of ^{56}Ni (Quimby et al. 2007; Gal-Yam et al. 2009), synthesized in a Pair Instability SN (PISN) (Barkat et al. 1967; Rakavy & Shaviv 1967). PISNe are the theoretical explosions of low metallicity and very massive main-sequence stars ($\sim 140\text{--}260 M_{\odot}$), ejecting several tens of solar masses of ^{56}Ni (Heger & Woosley 2002). These objects are expected to be common in the early Universe. The large amount of radioactive material ejected by PISNe can potentially power the extreme luminosities observed in SLSNe, however, some hydrogen-poor SLSNe fade too fast after peak to be consistent with the $^{56}\text{Ni} \rightarrow ^{56}\text{Co} \rightarrow ^{56}\text{Fe}$ decay chain, arguing against this power mechanism. Also the large opacity of iron-peak elements is expected to shift the emission towards near-infrared wavelengths (NIR), which is in conflict with the very blue continuum displayed by hydrogen-poor SLSNe (Dessart et al. 2012). Additional evidence against hydrogen-poor SLSNe being the result of PISNe, comes from the comparison between the observed spectra of SLSNe at nebular phase, which are dominated by emission lines of intermediate mass elements (Milisavljevic et al. 2013; Jerkstrand et al. 2017; Nicholl et al. 2016b, 2019; Mazzali et al. 2019), in contrast with the iron-peak element dominated nebular emission predicted for PISNe at this phase (see e.g., Dessart et al. 2012; Jerkstrand et al. 2016; Mazzali et al. 2019).

An alternative model to explain the light curve evolution of hydrogen-poor SLSNe invokes the spin-down of a highly magnetic newborn neutron star, a “magnetar”, that energises the SN ejecta (Maeda et al. 2007; Woosley 2010; Kasen & Bildsten 2010). The magnetar model was introduced by Maeda et al. (2007) to explain the peculiar double peaked and fast declining light curve of the Type Ib SN 2005bf. After the recognition of SLSNe as a new class, and using a small sample of well observed hydrogen-poor SLSNe, Insera et al. (2013) fitted an analytic magnetar model to their sample bolometric light curves and first showed that the power injection from the spin down of a magnetar can successfully reproduce the complete light curve evolution, including a light curve flattening at late times (~ 200 days), that cannot be explained by the ^{56}Co radioactive decay. More recently, Nicholl et al. (2017) presented a more sophisticated version of the magnetar model built-in the Modular Open Source Fit-

ter for Transients (MOSFiT; Guillochon et al. 2018). They applied their magnetar model to a large sample of hydrogen-poor SLSNe collected from the literature and showed that such magnetar model can explain the light curve evolution of many objects of this class.

Another alternative mechanism to power SLSN-I luminosity, is the SN ejecta-CSM interaction with a hydrogen and helium free CSM. For complete recent reviews on the SLSNe properties and their power sources see Gal-Yam (2019a) and Moriya et al. (2018).

Recently, the light curves of the hydrogen-poor SLSNe discovered in the course of the Palomar Transient Factory (PTF; De Cia et al. 2018), the Pan-STARRS1 Medium Deep Survey (PS1; Lunnan et al. 2018) and the Dark Energy Survey (DES; Angus et al. 2019) were presented and analysed. These surveys show that the low-luminosity tail of the SLSN population extends and overlaps in luminosity with the normal stripped envelope core collapse SN (CCSN) population. Although there is a continuous distribution in brightness from SNe Ic, Ic-BL to SLSNe-I, and rare examples of non-SLSNe powered by a magnetar exist (e.g., Maeda et al. 2007; Grayling et al. 2021), the dominant power mechanism seems to be different in the different SN populations. The well-sampled multi-band light curves provided by these surveys, confirmed the large diversity in the morphology of SLSN light curves, many of them showing bumps in their light curve evolution (see e.g., Nicholl et al. 2015; Smith et al. 2016; Yan et al. 2017).

The host galaxies of hydrogen-poor SLSNe are characterized by being low mass dwarf galaxies ($M_{\text{stellar}} < 2 \times 10^9 M_{\odot}$; e.g., Neill et al. 2011; Lunnan et al. 2014; Leloudas et al. 2015; Angus et al. 2016; Perley et al. 2016; Schulze et al. 2018), usually of irregular morphology with roughly half of the galaxies exhibiting a morphology that is either asymmetric, off-centre or consisting of multiple peaks (Lunnan et al. 2015), the latter being a possible signature of merging systems. SLSN host galaxies are clearly different from the galaxies hosting normal core-collapse SNe (CCSNe), which are more massive and in general exhibit spiral structure. SLSN-I host galaxies are also characterized by low metallicities ($Z \leq 0.5 Z_{\odot}$; e.g., Lunnan et al. 2014; Leloudas et al. 2015; Perley et al. 2016; Schulze et al. 2018), and by high specific Star Formation Rates (sSFR $\sim 10^{-9} \text{ yr}^{-1}$; e.g., Neill et al. 2011; Lunnan et al. 2014; Perley et al. 2016). The host galaxies of SLSNe-II are more diverse, showing a range of properties varying from low mass and metal poor dwarf galaxies, similar to the hosts of hydrogen-poor objects, to bright spiral galaxies similar to the hosts of normal CCSNe (Leloudas et al. 2015; Perley et al. 2016; Schulze et al. 2018).

Here we present and analyse observations of SN 2002gh obtained by the “Carnegie Type II Supernova Survey” (CATS, hereafter). This program was carried out at Las Campanas Observatory during 2002–2003 with the main purpose to study nearby ($z < 0.05$) SNe II. In the course of the CATS survey we included a handful of SNe of other classes. Remarkably, CATS results include observations of SN 2002ic, the first SN Ia showing interaction with a dense circumstellar medium (Hamuy et al. 2003), and SN 2003bg the first Type IIb hypernova (Hamuy et al. 2009). Here we add to these notable achievements, the observations of SN 2002gh, the second SLSN discovered after SN 1999as (Knop et al. 1999), for which its superluminous nature remained unnoticed for nearly two decades until now. In Section 2, we describe the data reduction and present the observations. In Section 3.1, we use Dark Energy Camera (Flaugher et al. 2015) archival images to identify and characterize the potential SN host galaxy. In Section 3.2 we characterize the light curves of SN 2002gh and in Section 3.3 we use blackbody fits to estimate the bolometric peak luminosity and the total radiated energy. In Section 3.3.1, we compare the bolometric light curve of SN 2002gh with

SLSNe from the PS1 and DES surveys, showing that SN 2002gh is among the brightest hydrogen-poor SLSNe. In Section 3.4 we explore the magnetar model and the radioactive decay of ^{56}Ni as potential power sources to explain the extreme luminosity of SN 2002gh. In Section 3.5, we identify spectral features in the SN 2002gh spectra, measure line velocities and compare with other well observed objects. Throughout this paper we adopt a Λ CDM cosmology with Hubble constant $H_0 = 70 \text{ km s}^{-1} \text{ Mpc}^{-1}$, total dark matter density $\Omega_M = 0.3$ and dark energy density $\Omega_\Lambda = 0.7$ in our calculations. Finally, in Section 4 we discuss and summarize our results.

2 OBSERVATIONS AND DATA REDUCTION

SN 2002gh was discovered by Wood-Vasey et al. (2002) on 2002 October 5 (MJD=52552.41) at an unfiltered magnitude of 19.3, in the course of the Nearby Supernova Factory. Previous to the SN discovery, a non-detection on 2001 December 14 reported by Wood-Vasey et al. (2002) places a 5σ upper limit on the SN magnitude of 21.2 mag.

The SN was located at $\alpha=03:05:29.46$ $\delta=-05:21:56.99$ (J2000.0). No host galaxy was clearly associated with SN 2002gh as shown in Fig. 1, but a nearby galaxy at $8''.6$ west and $6''.2$ south from the SN and at $z = 0.133$, indicated as G1 in Fig. 1, was originally identified as the possible host. However, after inspecting our highest signal-to-noise ratio spectra of SN 2002gh, we detected Mg II $\lambda\lambda$ 2796, 2803 doublet narrow absorption lines from the SN host galaxy at a redshift of $z = 0.3653 \pm 0.0005$ (see Fig. 2). This redshift value also makes the SN spectra consistent with other hydrogen-poor SLSNe-I as discussed below in Section 3.5.

The data were reduced using custom IRAF¹ scripts. A full description of the instruments characteristics and the reduction procedures can be found in Hamuy et al. (2006, 2009) and Cartier et al. (2014).

2.1 Photometry

We obtained more than 20 epochs of *BVI* optical photometry as part of the CATS project (Hamuy et al. 2009), beginning 10 days after the SN discovery. Our first photometric observations were obtained eight days before maximum light and extend to +200 rest-frame days after peak. The photometry is summarized in Table 1 and the SN light curves are shown in Fig. 3. The SN photometry was calibrated differentially relative to a set of 9 stars in the field as shown in Fig. 1. This local photometric sequence was calibrated in the Vega system on photometric nights with the Swope telescope at Las Campanas Observatory. The instrumental magnitudes of the local standard stars and of the SN were converted to the standard system using the colour terms and equations of Hamuy et al. (2009). Their average *BVRI* magnitudes are summarized in Table 2.

We interpolated the SN light curves using the PYTHON Gaussian process module implemented in SCIKIT-LEARN (Pedregosa et al. 2011). We present our interpolated light curves in Fig. 3. Then, we used the interpolated light curves to improve the flux calibration of the SN 2002gh spectra, presented in Section 2.2. After matching the spectra flux to the SN photometry we obtained additional photometry by computing synthetic photometry from the SN spectra (see Fig. 3), adding relevant photometric information in the *R* band. The synthetic

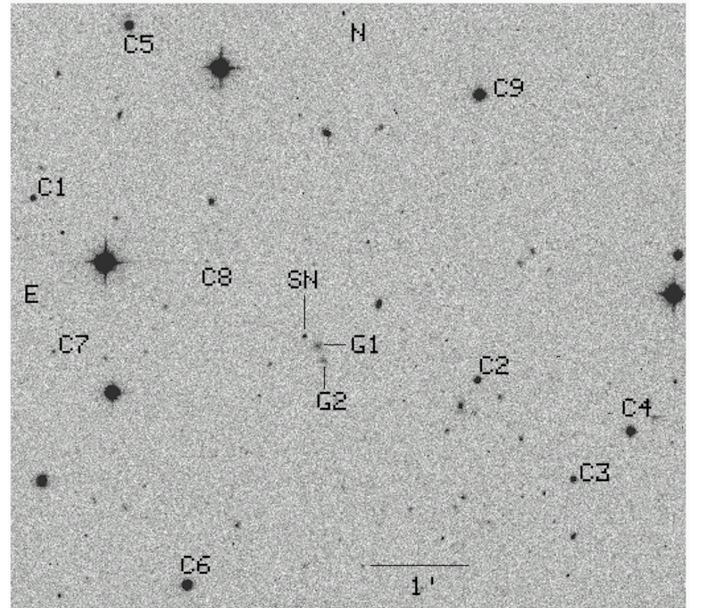


Figure 1. Field of SN 2002gh observed with the Swope 1 m telescope in the V-band when the SN was near maximum light. North is up and east is to the left. We label SN 2002gh along with nine comparison stars used to derive the differential photometry of the SN. Two nearby galaxies to the south-west of the SN are indicated as G1 and G2. Galaxy G1 has a redshift of 0.133 and was originally identified as the possible host. The image scale is shown with a horizontal line near the bottom.

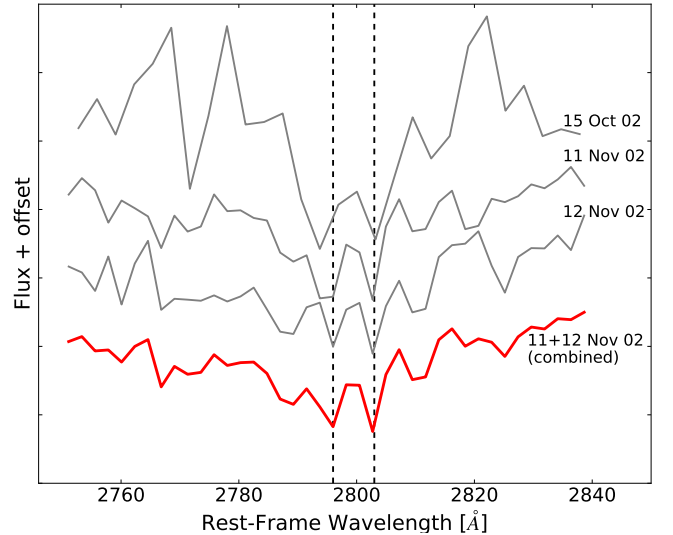


Figure 2. Spectra of SN 2002gh around the region of Mg II $\lambda\lambda$ 2796, 2803 lines, selected for their high signal-to-noise ratio and good resolution. The grey spectra were obtained on different nights and with different instruments. In all of them we detect weak Mg II $\lambda\lambda$ 2796, 2803 doublet absorption lines (black-dashed lines) at a redshift of 0.3653 ± 0.0005 . At the bottom of the panel we show the average spectrum from November 11 and 12, which were obtained with the same instrument on consecutive nights.

¹ Image Reduction Analysis Facility, distributed by the National Optical Astronomy Observatories (NOAO), which is operated by AURA Inc., under cooperative agreement with NSF.

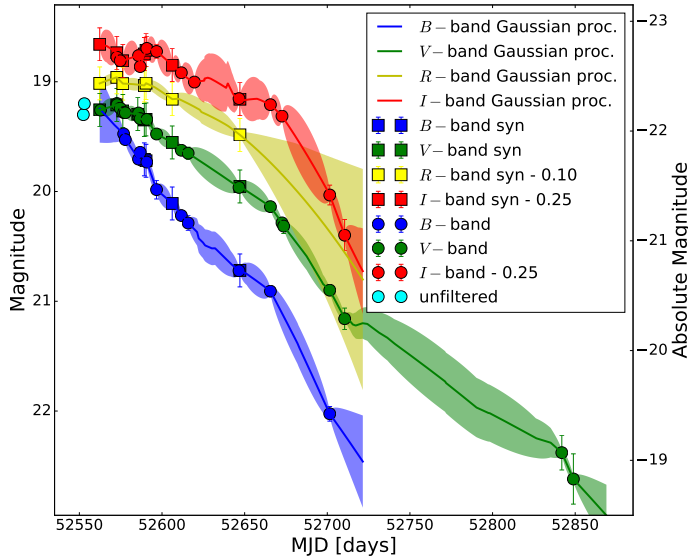


Figure 3. Optical light curves of SN 2002gh. We present *BVI* photometry obtained in the course of the CATS project (Hamuy et al. 2009), unfiltered photometry reported by Wood-Vasey et al. (2002), and *BVRI* synthetic photometry computed from the spectra after matching them to the interpolated photometry. The legend is presented on the top right of the figure.

photometry was computed as it is described in Bessell (2005), using the Johnson-Cousins *BVRI* response functions of Bessell (1990). The difference between the synthetic photometry and the interpolated and observed photometry is always below 5%, but we conservatively quote an uncertainty of 0.15 mag for the computed synthetic photometry.

2.2 Spectroscopy

A total of ten spectra of SN 2002gh were obtained, spanning from -8 to +54 rest-frame days relative to the estimated bolometric maximum. We summarize spectroscopic observations in Table 3, and the spectral sequence is presented in Fig. 4. We improved the flux calibration by using interpolated photometry (see Section 2.1) and we fitted a blackbody model to the spectral sequence to estimate the blackbody radius (R_{bb}) and temperature (T_{bb}).

3 ANALYSIS

3.1 Host galaxy characterization

The field of the SN explosion has been covered by several modern digital surveys over the past decades. With the aim of identifying and characterize the SN 2002gh host galaxy, we searched for host galaxy candidates close to the SN position in these deep surveys. The nearest astronomical source to the SN site detected by both SDSS and Pan-STARRS is galaxy G1 shown in Fig. 1, and already discussed in Section 2.

We queried the NOAO archive for DECam archival frames containing the SN region and after inspecting them, we noticed some faint emission close to the SN site on some of the individual DECam frames. However, the number of counts is too low to claim a detection on these individual frames. Therefore, to sum all possible photons, we stacked all *griz* frames for each individual filter, and we

also made a multi-band image stack with all the *griz* frames using SWARP (Bertin et al. 2002). Figure 5 shows the result of the multi-band *griz* image stack and a colour composite image made of the individual *g*, *r*, *z* stacks.

On the multi-band image stack, we detected an extended object at $\sim 10\sigma$ flux level above the background with centroid equatorial coordinates of $\alpha = 03:05:29.47$ $\delta = -05:21:57.08$ (J2000) located $0''.13$ south-east from the SN location corresponding to a projected distance of 0.67 kpc, at the redshift of the SN. We did not detect this source in the *i*-band image stack. In the *g*-band deep stack, we detected this source at $\sim 9\sigma$ level. On the *r*-band deep stack we detected three faint sources within $\sim 1''.5$ of the SN position. The first source is detected at $\sim 6\sigma$ and the peak of the emission is $1''.01$ or at a projected distance of 5.14 kpc north-east from the galaxy centroid measured in the multi-band image stack. The central source is detected at $\sim 10\sigma$ level and is located $0''.08$ or at a projected distance of 0.44 kpc to the north-west of the galaxy centroid, this is essentially coincident with the multi-band image centroid. Finally, the third source is detected at $\sim 8\sigma$ and the peak is $0''.96$ or at a projected distance of 4.90 kpc to the south-west of the galaxy centroid. Although the latter source is not detected as a different source in the *g*-band, it is clear that there are two emission peaks in the *g*-band image stack, one coincident with the main central source and one coincident with the south-west source. The three sources detected in the *r*-band can be distinguished in the colour composite image on Fig. 5. In the *z*-band we detected a source at the $\sim 6\sigma$ level with the peak located $0''.36$ or at a projected distance of 1.82 kpc to the north-east from the multi-band galaxy centroid. Again this is essentially coincident with the main multi-band image centroid. The *z*-band source is very weak and does not show evidence of structured emission. Although the small projected distance between the host galaxy candidate reported here and the SN is a strong reason to think that this is the SN host, further spectroscopic confirmation of the galaxy redshift is required for a solid association. The multi-peak morphology found in the SN 2002gh's host candidate is common in hydrogen-poor SLSN host galaxies. Analysing *Hubble Space Telescope* images, Lunnan et al. (2015) found that roughly half of the hydrogen-poor SLSN host galaxies exhibit a morphology that is either asymmetric, off-centre or consisting of multiple peaks. Recently, Ørum et al. (2020) found that hydrogen-poor SLSN host galaxies are often part of interacting systems, with $\sim 50\%$ having at least one major companion within 5 kpc.

Under the assumption that this is the SN host, we note that at this redshift the usual emission lines of SLSN-I host galaxies, such as [O II] $\lambda\lambda$ 3726, 3729 doublet emission lines lie within the *g* band, the $H\beta$ and the [O III] $\lambda\lambda$ 4959, 5007 doublet emission lines lie within the *r* band, and the $H\alpha$ and [S II] $\lambda\lambda$ 6717, 6731 doublet emission lines lie within the *z* band. These emission lines are strong in regions with recent or ongoing star-formation, in particular in Extreme Emission Line Galaxies (EELGs; e.g. Cardamone et al. 2009; Atek et al. 2011; Amorín et al. 2014, 2015), and therefore the peaks detected could be tracing regions of strong star-formation within the irregular host or could simply mean that these are different dwarf galaxies in the merging process. Leloudas et al. (2015) showed that hydrogen-poor SLSNe hosts are found in environments where the gas is strongly ionized, more than in stripped CCSN hosts, and have stronger [O III] λ 5007 emission lines compared to the hosts of other transients types, but comparable to EELGs.

We performed aperture photometry using SExtractor (Bertin & Arnouts 1996), and we calibrated against *griz* magnitudes of stars C2, C3, C4, C6 and C7 in Fig. 1 from SDSS. We summarize the host galaxy photometry in Table 4.

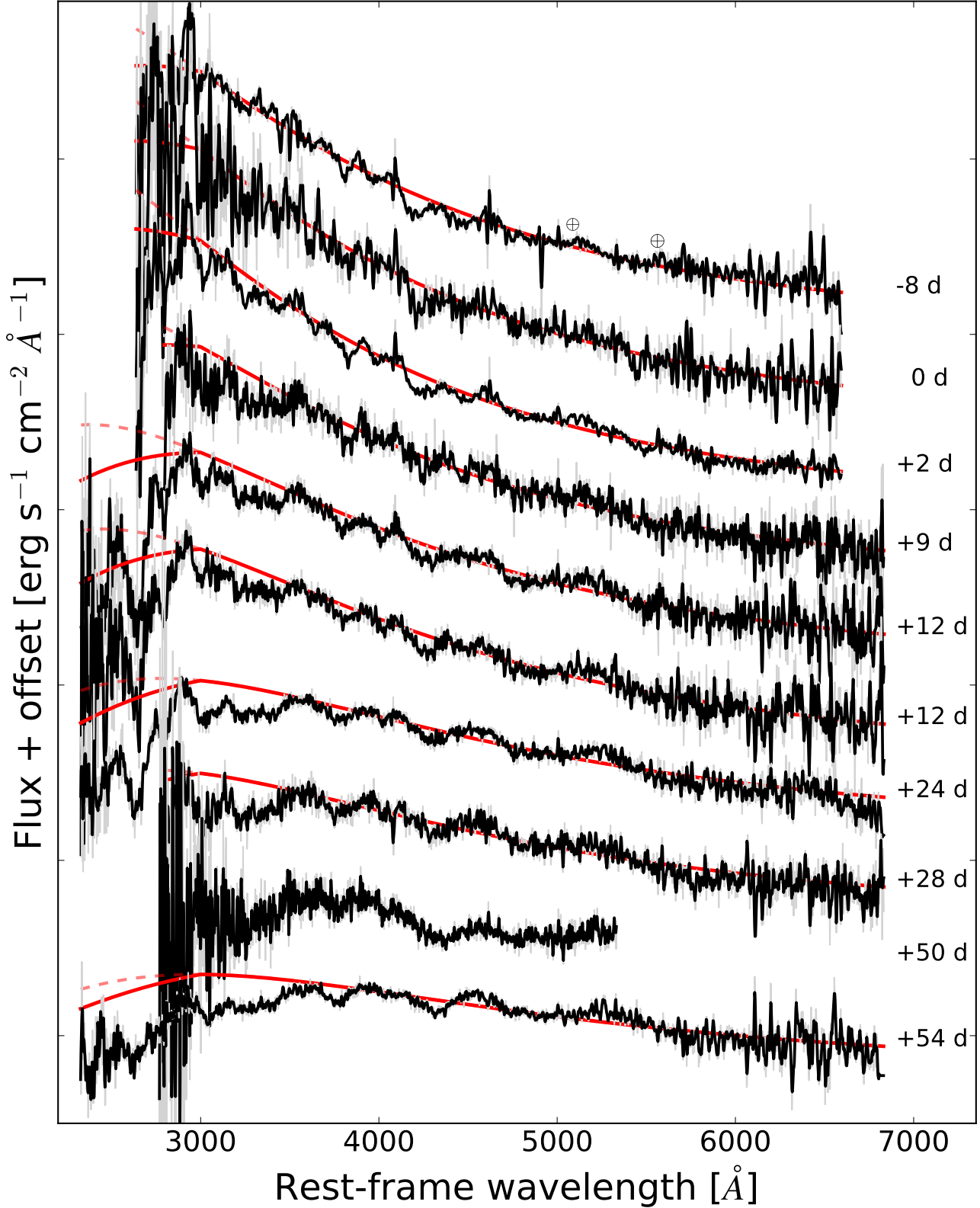


Figure 4. Spectroscopic sequence of SN 2002gh. The spectra have been mangled in order to match the *BVI* interpolated photometry at their corresponding epoch, yielding accurate flux calibration. Then we corrected the spectra by a Galactic reddening of $E(B - V) = 0.0593$ mag (Schlafly & Finkbeiner 2011) in the line-of-sight using the Cardelli et al. (1989) reddening law with $R_V = 3.1$. Finally, the spectra are corrected by the host galaxy redshift to place the spectra in the rest-frame system. The red solid lines correspond to modified blackbody fits to the SN spectra with a linear flux suppression below the “cutoff” wavelength at 3000 Å, and the dashed red lines correspond to the normal blackbody without flux suppression. On the right we give the phase relative to the estimated rest-frame time since bolometric maximum.

Table 1. Optical photometry of SN 2002gh

Date UT	MJD	<i>B</i>	<i>V</i>	<i>I</i>	Tel.
2002-10-15	52562.8	–	19.258(0.010)	–	LDSS-2/Baade
2002-10-25	52572.7	–	19.198(0.022)	19.026(0.028)	CCD/Swope
2002-10-25	52572.8	–	19.209(0.016)	–	LDSS-2/Baade
2002-10-27	52574.7	–	19.241(0.015)	19.059(0.036)	CCD/CTIO 0.9 m
2002-10-29	52576.8	19.475(0.017)	19.281(0.014)	–	LDSS-2/Baade
2002-10-30	52577.8	19.527(0.020)	19.283(0.014)	–	WFCCD/du Pont
2002-11-07	52585.8	–	19.316(0.024)	–	WFCCD/du Pont
2002-11-07	52585.8	19.705(0.031)	19.285(0.018)	19.012(0.054)	CCD/Swope
2002-11-08	52586.8	19.643(0.016)	19.336(0.014)	19.112(0.038)	CCD/Swope
2002-11-12	52590.8	19.732(0.039)	19.343(0.032)	18.946(0.111)	CCD/Swope
2002-11-18	52596.7	19.983(0.085)	19.476(0.044)	18.974(0.061)	CCD/Swope
2002-12-03	52611.7	20.219(0.019)	19.624(0.023)	19.168(0.037)	WFCCD/du Pont
2002-12-07	52615.8	20.287(0.066)	19.651(0.055)	–	CCD/Swope
2002-12-11	52619.6	–	–	19.253(0.026)	CCD/Swope
2003-01-07	52646.6	20.722(0.033)	19.963(0.020)	19.404(0.053)	CCD/Swope
2003-01-26	52665.6	20.908(0.037)	20.138(0.021)	19.459(0.035)	CCD/Swope
2003-02-02	52672.6	–	20.286(0.024)	19.563(0.039)	CCD/Swope
2003-02-03	52673.6	–	20.315(0.068)	–	WFCCD/du Pont
2003-03-03	52701.5	22.026(0.067)	20.899(0.046)	20.282(0.090)	WFCCD/du Pont
2003-03-12	52710.5	–	21.159(0.097)	20.648(0.142)	WFCCD/du Pont
2003-07-21	52841.9	–	22.379(0.158)	–	CCD/Swope
2003-07-28	52848.9	–	22.619(0.229)	–	CCD/Swope

Numbers in parentheses correspond to 1σ statistical uncertainties.

Table 2. *BVR* photometric sequence around SN 2002gh.

Star	R.A.	Dec	<i>B</i>	<i>V</i>	<i>R</i>	<i>I</i>
C1	03:05:40.66	−05:20:36.77	18.997(0.040)	18.104(0.013)	18.450(0.017)	17.042(0.009)
C2	03:05:22.31	−05:22:21.09	18.466(0.042)	17.572(0.015)	17.936(0.015)	16.529(0.009)
C3	03:05:18.29	−05:23:20.11	18.876(0.019)	17.799(0.025)	18.106(0.015)	16.425(0.015)
C4	03:05:16.00	−05:22:50.10	16.684(0.015)	15.955(0.019)	–	15.029(0.010)
C5	03:05:36.90	−05:18:49.67	17.067(0.037)	16.067(0.015)	16.399(0.015)	15.005(0.008)
C6	03:05:33.99	−05:24:30.93	16.094(0.031)	15.429(0.024)	15.987(0.015)	14.656(0.010)
C7	03:05:39.72	−05:22:11.62	22.764(0.538)	21.385(0.093)	21.892(0.366)	18.795(0.026)
C8	03:05:33.46	−05:21:12.59	22.869(0.339)	21.296(0.162)	20.873(0.146)	18.665(0.024)
C9	03:05:22.52	−05:19:26.92	15.590(0.031)	14.903(0.014)	15.416(0.015)	–

Numbers in parentheses correspond to 1σ statistical uncertainties.

Table 3. Summary of Spectroscopic Observations of SN 2002gh.

Date UT	MJD	Phase (days)	Instrument/ Telescope	Wavelength Range (Å)
2002-10-15	52562.3	−8.0	LDSS-2/Baade	3600 – 9000
2002-10-25	52572.6	−0.5	LDSS-2/Baade	3600 – 9000
2002-10-29	52576.3	+2.2	LDSS-2/Baade	3600 – 9000
2002-11-07	52585.3	+8.8	WFCCD/du Pont	3820 – 9330
2002-11-11	52589.3	+11.7	B&C Spec./Baade	3180 – 9315
2002-11-12	52590.3	+12.4	B&C Spec./Baade	3180 – 9315
2002-11-28	52606.2	+24.0	B&C Spec./Baade	3180 – 9312
2002-12-03	52611.2	+27.8	WFCCD/du Pont	3820 – 9330
2003-01-03	52642.2	+50.5	Mod. Spec./du Pont	3780 – 7280
2003-01-08	52647.1	+54.0	B&C Spec./Baade	3180 – 9280

3.2 Light curve characterization

SN 2002gh was discovered a few weeks before peak brightness, and our observations begin about a week before maximum in rest-frame. We distinguish four phases in the light curve evolution of SN 2002gh

Table 4. DECam *griz* photometry for the SN 2002gh host galaxy.

Filter	mag	Abs. mag
<i>g</i>	24.3(0.2)	−17.3
<i>r</i>	23.5(0.1)	−18.2
<i>i</i>	>24.1	>−17.5
<i>z</i>	23.3(0.3)	−18.3

Numbers in parentheses correspond to 1σ statistical uncertainties.

in Fig. 3. The first phase corresponds to the light curve evolution close to maximum light, a second phase of decline post-maximum until ≈ 70 days after maximum, a third phase of faster decline between days 70–110, and a fourth phase between 110–200 days, for which we only have observations in the *V*-band.

The optical observations presented here begin shortly before maximum brightness in the *VRI* bands, and after *B*-band maximum. The *I*-band observations show a bumpy structure close to peak, which seems to be caused by a lower signal-to-noise photometry in this band. To estimate the epoch and the brightness at maximum light in

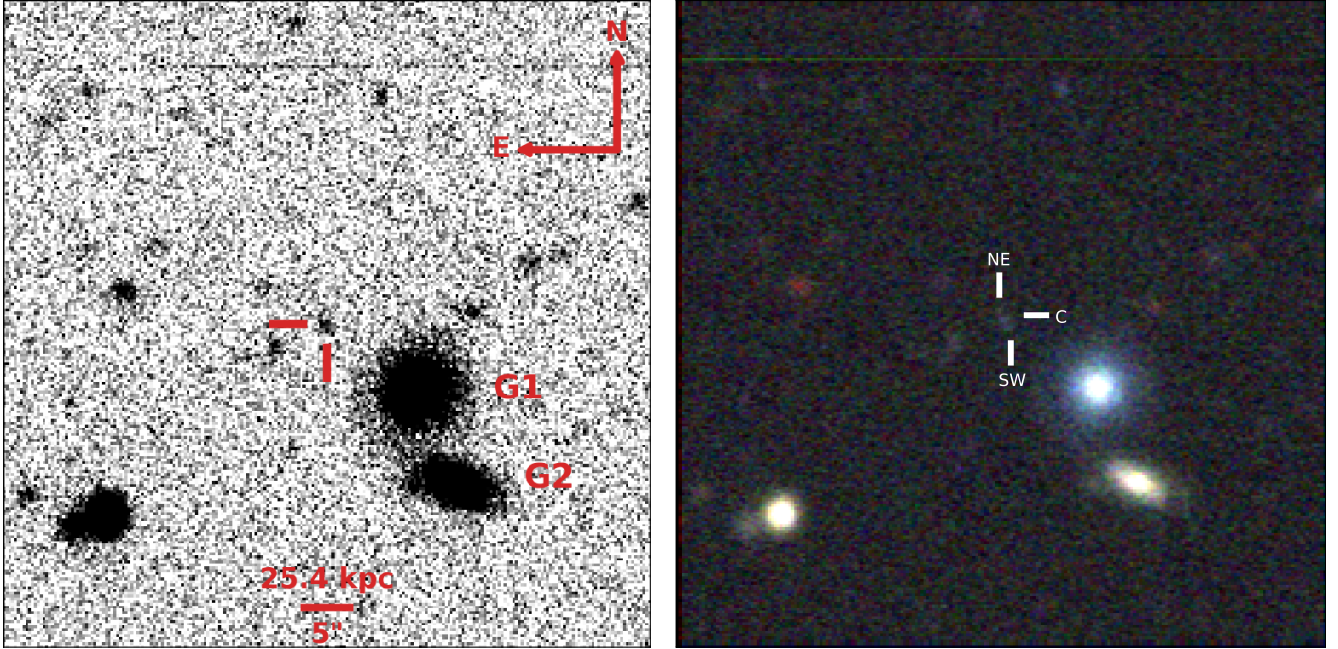


Figure 5. In the left panel, we present a greyscale image centred on the position of SN 2002gh, resulting from stacking all the *griz* DECam frames available. We indicate the host galaxy position with red tick marks, and we label the foreground galaxies G1 and G2. In the right panel, we present a *grz* colour image composite made of deep image stacks in these filters. In the colour image, the position of the north-east, central and south-west faint distinct components detected in the *r* band associated to potential host galaxy of SN 2002gh, are indicated with a white tick marks. The field-of-view of both images is $1'0 \times 1'0$, and at the bottom of the left panel we give as reference the projected physical distance of $5''0$ at the SN redshift.

VRI bands, a low order polynomial was fitted the light curves around peak brightness. An upper limit on the MJD of the *B*-band maximum and the in the magnitude at this epoch was placed. These values are summarized in Table 5, where a Monte Carlo simulation was used to estimate the uncertainty in these quantities.

A first order polynomial was fitted to the post-peak phases, and the goodness-of-fit of these linear models was estimated by computing χ^2_V and the root mean squared (*rms*) of the fit. Inspecting the fit residuals, we find that a first order polynomial is a suitable model over these limited ranges of time. The values for the decline rates, χ^2_V , and the *rms* are summarized in Table 6.

During this second phase, spanning from after peak brightness to 77 days after maximum light, the SN luminosity declined more rapidly in the bluer bands with decline rates of 2.39, 1.44, 1.09 and 0.79 mags/100 days in *B*, *V*, *R*, *I*, respectively. In particular, we notice that the *B*-band declined three times faster than the *I*-band, at the 10σ level, pointing to a rapid decrease of the UV emission after maximum due to a decrease of the ejecta temperature, as a consequence of which there is an increase in the strength of the absorption lines mainly due to Fe II and intermediate-mass elements (IME's), as we will discuss below (Section 3.5).

In the third phase, from 70 to 110 days after maximum brightness, we found that the decline rates increase to 4.24, 2.95 and 3.32 mags/100 days in *B*, *V*, *I* bands, respectively. This is an increase by a factor of 1.8, 2.0 and 4.2, respectively, compared to the decline rates in previous phase in the same bands. Note that the rapid decline in the *B* band, measured using only two observations, is larger by 1.29 ± 0.34 mag/100 days or by 4σ than the *V*-band decline rate at this phase. This implies a rapid fading of the near-UV emission. The *V* and *I* decline rates are similar at this phase within 1σ level. We

Table 5. Peak magnitude information for SN 2002gh.

Filter	MJD peak (days)	Peak magnitude	Peak abs. magnitude
<i>B</i>	≤ 52576.8	≤ 19.48	≤ -22.21
<i>V</i>	52569.8(1.2)	19.23(0.02)	-22.40
<i>R</i>	52574.6(6.3)	19.09(0.15)	-22.50
<i>I</i>	52594.8(3.4)	18.98(0.06)	-22.57

Numbers in parentheses correspond to 1σ statistical uncertainties.

notice that these decline rates are faster than the expected decline of ~ 1 mag/100 days for a SN powered by the radioactive decay of ^{56}Co , the daughter product of ^{56}Ni . The decline rate in the *V* band in the fourth phase was measured by fitting a linear model to the last three photometric observations in this band, finding a value of 1.33 ± 0.17 mags/100 days. Although there is a gap of nearly 100 days between the first point and the last two points, the *V* band reduced its decline rate to less than half of its previous phase value, at the 7.5σ level. This show evidence of a flattening in the light curve at this late phase, with the average decline rate over the course of this phase now more consistent with ^{56}Co decay.

3.3 Blackbody fits, bolometric and pseudo-bolometric light curves

The spectral energy distribution (SED) of hydrogen-poor SLSNe can be well described by a blackbody model from the time of explosion to a few days or weeks after maximum light (e.g., Nicholl et al. 2017). After maximum light, the SLSNe emission becomes progressively

Table 6. Decline rates in the optical bands for SN 2002gh.

Filter	Dec. rate phase 1 (mag/100 days)	χ^2_{ν}	rms (mag)	n_{obs}	Dec. rate phase 2 (mag/100 days)	χ^2_{ν}	rms (mag)	n_{obs}	Dec. rate phase 3 (mag/100 days)	χ^2_{ν}	rms (mag)	n_{obs}
<i>B</i>	2.39(0.04)	5.15	0.020	14	4.24(0.29)	–	–	2	–	–	–	–
<i>V</i>	1.44(0.03)	0.71	0.006	14	2.95(0.17)	0.13	0.013	5	1.33(0.17)	0.38	0.064	3
<i>R</i>	1.09(0.44)	0.01	0.007	4	–	–	–	–	–	–	–	–
<i>I</i>	0.79(0.08)	1.22	0.022	7	3.32(0.29)	1.22	0.045	4	–	–	–	–

Numbers in parentheses correspond to 1σ statistical uncertainties.

dominated by broad features similar to broad-line SNe Ic (Liu et al. 2017), and then enter progressively in the nebular phase (Jerkstrand et al. 2017; Nicholl et al. 2016b, 2019).

To estimate the radius and the temperature of the SN ejecta we fitted a modified blackbody model to the interpolated *VRI* photometry of SN 2002gh corrected by Galactic extinction. The conversion from magnitudes in the Vega photometric system to monochromatic fluxes was done using the zero points listed in the Table A2 of Bessell et al. (1998). The modified blackbody function employed to compute the SN bolometric luminosity, it corresponds to the Planck function with a linear flux suppression below the “cutoff” wavelength at 3000 Å as shown in Fig. 4 and it is described in the Appendix. To complement *V* and *I* bands in the blackbody fits, we used *R*–band synthetic photometry and extrapolated this band by about 50 days using the Gaussian process model shown in Fig. 3. We compared fits obtained from *VRI* and *VI* photometry, and found that both methods yield similar results. We noticed that the addition of *R*–band synthetic photometry brings the blackbody parameters closer to the values estimated from fitting a blackbody to the SN spectra (see Figs. 4 and 6).

We did not include *B*–band photometry in our blackbody fits as this band is affected by strong absorptions from about ten days after maximum, as can be seen in Fig. 4 and discussed in Sections 3.2 and 3.5. To study this effect, we compared the blackbody parameters obtained by fitting a blackbody model to the *BVRI* and to the *VRI* photometry. At early times ($<+12$ days) the *B*–band emission is not significantly affected by strong spectral features and the derived blackbody parameters obtained including *B*–band photometry yield an excellent match with the blackbody computed using *VRI* photometry and with the SN spectra. After this, the *B* band becomes progressively affected by the decrease in the ejecta temperature (Section 3.5), evidencing clear differences between the blackbody temperature and radius computed with and without including the *B*–band. However, in all cases we find a good agreement in the bolometric luminosity. We decided to use *VRI* to perform the blackbody fits because it yields the most reliable and consistent blackbody parameters at all epochs.

The blackbody fits were performed by minimizing χ -square and assuming a luminosity distance of 1,953.6 Mpc, which yielded three physical parameters for each epoch: the blackbody temperature (T_{bb}), radius (R_{bb}) and the bolometric luminosity. To estimate the uncertainty in these parameters a Monte Carlo simulation was performed, where we simulate 15,000 times a new set of photometric points assuming a Gaussian distribution with the standard deviation equal to the photometric uncertainty, and the blackbody parameters were re-computed obtaining a distribution for each of them. From the distribution obtained for T_{bb} and R_{bb} , lower and upper 1σ limits were computed (Fig. 6).

We computed bolometric (L_{bol}) and pseudo-bolometric (UVOIR; L_{UVOIR}) light curves. To compute the L_{UVOIR} , the blackbody emission was integrated from 3000 Å to 20,000 Å (see Fig. 6). As for

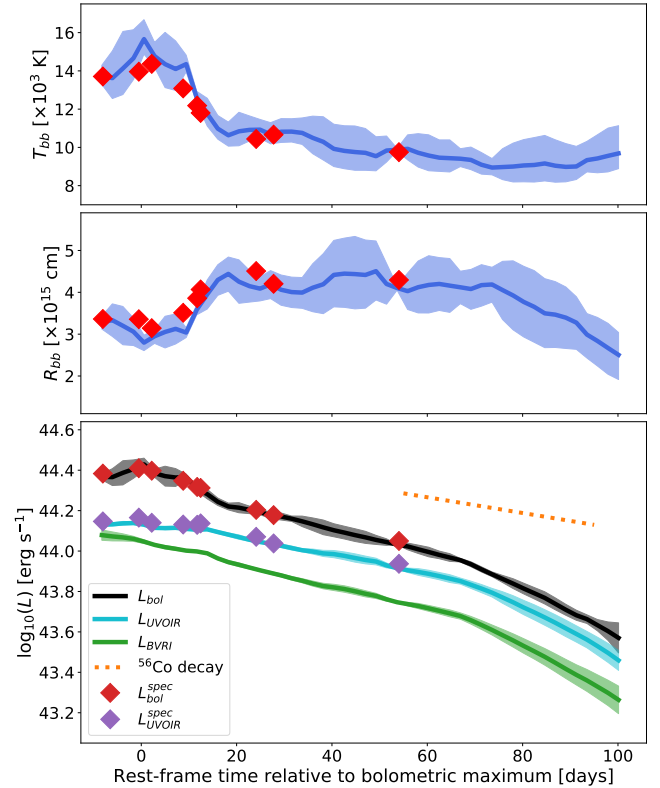


Figure 6. Blackbody parameters, bolometric and pseudo-bolometric light curves for SN 2002gh. In the top and middle panel we present the blackbody temperature T_{bb} and radius R_{bb} obtained from the blackbody fits to the *VRI* interpolated photometry of SN 2002gh (blue line) and to the spectra (red diamonds; see Fig. 4). In the bottom panel, we present the L_{bol} (black), L_{UVOIR} (cyan) and L_{BVRI} (green) light curves and compare them with the decline rate of ^{56}Co . We also present the individual points computed from the blackbody fits to the spectra for L_{bol} (red diamonds) and L_{UVOIR} (purple diamonds).

the blackbody parameters, a Monte Carlo approach was employed to estimate the uncertainty of the bolometric and UVOIR light curves. The observed optical luminosity (L_{BVRI}) was estimated summing the emission in the *BVRI* bands (Fig. 6).

The peak of the bolometric emission was on MJD = 52573.3 \pm 3.0 days with a luminosity of $2.6 \pm 0.2 \times 10^{44}$ erg s $^{-1}$ ($\log_{10}(L_{bol}^{peak}) \approx 44.4$). This value places SN 2002gh among the brightest SLSNe, with a handful of objects reaching brighter peak bolometric luminosities as we discuss below. The peak observed luminosity was on MJD = 52562.0 \pm 2.0 days with $1.2 \pm 0.07 \times 10^{44}$ erg s $^{-1}$ ($\log_{10}(L_{BVRI}^{peak}) \approx 44.1$). The ratio between the bolometric

Table 7. Luminosity decline rates of SN 2002gh.

Light curve	Dec. rate at +15 d <ph <+70 d (mag/100 days)	Dec. rate at ph >+70 d (mag/100 days)
L_{bol}	1.49(0.06)	2.79(0.20)
L_{UVOIR}	1.16(0.02)	2.96(0.26)
L_{BVRI}	1.38(0.02)	2.82(0.31)

Numbers in parentheses correspond to 1σ statistical uncertainties.

luminosity and the luminosity observed in the optical bands is $L_{\text{bol}}^{\text{peak}}/L_{\text{BVRI}}^{\text{peak}} = 2.2 \pm 0.1$.

We estimate that the total radiated energy from -8 to $+100$ days is 1.2×10^{51} erg, and a total radiated energy observable in the optical bands of 6.1×10^{50} erg, over the same period of time. These values represent a lower limit to the energy emitted by the SN.

The decline rates of the bolometric and pseudo-bolometric light curves over the phase from 15 to 70 days and from 70 days to the end of the light curves (≈ 100 days) were measured. These ranges are roughly equivalent to the second and third phases analysed in the previous section, however, here we use interpolated light curve values while in Section 3.2 we used individual photometric observations. These luminosity decline rates in magnitudes declined over 100 days are summarized in Table 7. Note that the decline rate during the first phase (15 to 70 days) is more rapid than the decline rate expected for a light curve powered by the $^{56}\text{Co} \rightarrow ^{56}\text{Fe}$ decay, but it could be still consistent with the ^{56}Co decay. However, the decline rate measured for the second phase ($t > +70$ days) is nearly 3 times faster than the expected decline rate for a ^{56}Co powered light curve. This suggests that the decay of ^{56}Ni is not the main power source of SN 2002gh. This will be discussed in detail in Section 3.4.2 below.

Despite that the L_{bol} computation assumes a blackbody SED, which does not hold at all epochs, particularly at late phases, L_{bol} and L_{BVRI} decline rates are in very good agreement, specially at $t > +70$ days. Also note that over similar phases, the L_{bol} decline rates are very similar to the V -band decline rates presented in Table 6.

3.3.1 Luminosity comparison

It has been shown that SN 2002gh is a bright SN belonging to the SLSN class. However, at this point is unclear how bright it is relative to other SLSNe. In this section, the bolometric light curve of SN 2002gh is compared with a large sample of SLSNe, placing this object in the context the SLSN population as a whole. To this end, a set of bolometric light curves are computed, using photometry from spectroscopically confirmed hydrogen-poor SLSNe from Pan-STARRS1 (PS1; Lunnan et al. 2018) and the Dark Energy Survey (DES; Angus et al. 2019). The large PTF SLSN sample (De Cia et al. 2018) is not included in this analysis as their multi-band photometry is not uniform across their entire sample, thus making difficult the construction of a homogeneous set of bolometric light curves. Well observed objects from the literature are not included in our sample of bolometric light curves either, as individual objects suffer from biases sometimes difficult to account for. Note that the PS1 and DES SLSN samples suffer from spectroscopic selection biases, inherent to any spectroscopic sample, which are discussed by Lunnan et al. (2018) and Angus et al. (2019), respectively. Nevertheless, these two SLSN samples represent a well characterized data set, with well defined photometric systems, providing uniform and deep multi-band photometry (*griz*), thus perfect for constructing bolometric light curves.

The redshift ranges are $0.3 \lesssim z \lesssim 1.6$ for the PS1 sample and $0.2 \lesssim z \lesssim 2.0$ for the DES sample.

The rest-frame optical and NIR is the spectral region of choice for fitting a blackbody SED to SLSNe. For this reason we restrict ourselves to construct bolometric light curves for objects at $z \lesssim 1.2$. This choice is justified in the Appendix.

In the left-panel of Fig. 7, the bolometric light curves of 28 SLSNe-I, 11 from PS1 and 17 from DES, are presented and compared with the bolometric light curve of SN 2002gh. As can be observed SN 2002gh reaches one the largest maximum luminosities of this sample, with only two SNe from PS1 reaching similar values. Note that PS1 SLSNe are concentrated in a brighter region of the plot, having a maximum bolometric luminosity range of $\log_{10}(L_{\text{bol}}) = 43.5 - 44.4$. The DES SLSNe span a wider luminosity range with $\log_{10}(L_{\text{bol}}) = 43.25 - 44.3$. This is likely explained in part by the fact that the DES survey limiting magnitude, in terms of photometry and spectroscopy, reaches nearly 1 mag fainter than the PS1 survey. As can be noticed in the figure there is a large diversity in the shape of the light curves, with some objects having early bumps and others showing bumps after maximum light. We also find a large diversity in the rise times with objects having rise times of about 30 days and others showing broader light curves, with PS1-14bj being an extreme object with a rise time of more than 100 days. No apparent relation between the peak luminosity and the light curve shape is found.

In the right-panel of Fig. 7 the luminosity light curves for PS1 and DES SLSNe constructed by adding the emission detected in the optical bands are presented. Here the sample is not restricted to objects with $z \lesssim 1.2$, thus all PS1 and DES objects are included. SN 2002gh is again among the brightest SLSNe, only PS1-13or ($z = 1.53$) reaches a brighter maximum luminosity. Here again PS1 SLSNe are concentrated in a brighter region compared with DES objects, which are distributed over a wider luminosity range.

In Fig. 8 the maximum bolometric luminosity distribution is presented for spectroscopically confirmed hydrogen-poor SLSNe from PS1 and DES. This distribution includes all possible PS1 and DES objects, 37 SLSNe in total. For objects at $z > 1.2$, we estimate the maximum bolometric luminosity using the heuristic $L_{\text{bol}}/L_{\text{obs}}$ scaling relation described in the Appendix. Only PS1-10awh ($z = 0.909$), PS1-11bam ($z = 1.565$), PS1-13or ($z = 1.53$), and DES15E2mlf ($z = 1.861$) have a similar or brighter maximum luminosity than SN 2002gh. This figure confirms that SN 2002gh lies at the extreme of the distribution, only comparable to the most luminous objects in a sample of 37 SLSNe, which includes the most distant and luminous objects detected to date.

3.4 Power source

In this Section the magnetar model together with radioactive decay of ^{56}Ni are explored as possible sources to power the extreme luminosity of SN 2002gh.

3.4.1 Magnetar model

A popular model to explain the extreme luminosities of hydrogen-poor SLSNe is the power injection from the spin down of a newborn magnetar formed in the SN explosion. Under the assumption that SN 2002gh is powered by the spin down of a magnetar, here we use the magnetar model implemented by Nicholl et al. (2017) to fit the photometry of SN 2002gh using two methodologies: 1) the Modular Open Source Fitter for Transients (MOSFiT; Guillochon et al. 2018) that uses the SN photometry as input, and 2) our PYTHON implementation of the model to fit the bolometric light curve directly.

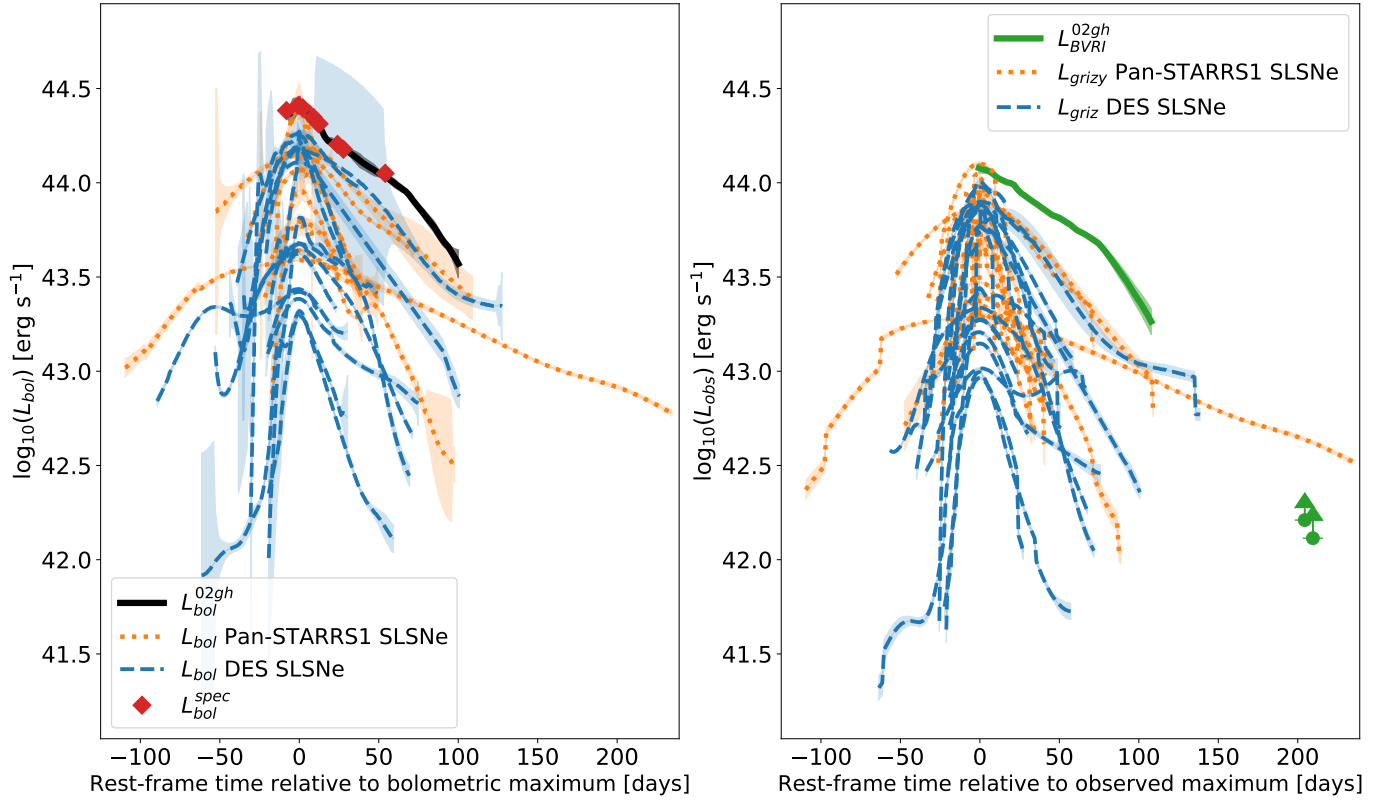


Figure 7. Bolometric and observed luminosity light curve comparison between SN 2002gh and the spectroscopically confirmed SLSNe from Pan-STARRS1 (Lunnan et al. 2018) and DES (Angus et al. 2019). In the left panel, we present the bolometric light curves and in the right panel we present the emitted luminosity detected in the optical bands. In the Appendix we describe our methodology to compute bolometric and observed luminosity light curves in detail.

Here we briefly summarize the main analytic expressions of the magnetar model of Nicholl et al. (2017). We refer the reader to this article and the references therein for a detailed description of the model. The magnetar energy input is:

$$F_{\text{mag}}(t) = \frac{E_{\text{mag}}}{t_{\text{mag}}} \frac{1}{(1 + t/t_{\text{mag}})^2}, \quad (1)$$

where the magnetar rotational energy is

$$E_{\text{mag}} = 2.6 \times 10^{52} \left(\frac{M_{\text{NS}}}{1.4 M_{\odot}} \right)^{3/2} \left(\frac{P_{\text{spin}}}{1 \text{ ms}} \right)^{-2} \text{ erg}, \quad (2)$$

and the magnetar spin down timescale is given by

$$t_{\text{mag}} = 1.3 \times 10^5 \left(\frac{M_{\text{NS}}}{1.4 M_{\odot}} \right)^{3/2} \left(\frac{P_{\text{spin}}}{1 \text{ ms}} \right)^2 \left(\frac{B}{10^{14} \text{ G}} \right)^{-2} \text{ s}. \quad (3)$$

The output SN luminosity is calculated using the traditional analytic solution of Arnett (1982), where in this case the SN energy source is $F_{\text{mag}}(t)$ and the analytic expression takes the following form:

$$L_{\text{SN}}(t) = e^{-(t/t_{\text{diff}})^2} (1 - e^{-At^{-2}}) \int_0^t 2 F_{\text{mag}}(t') \frac{t'}{t_{\text{diff}}} e^{(t'/t_{\text{diff}})^2} \frac{dt'}{t_{\text{diff}}}, \quad (4)$$

where the diffusion timescale is given by

$$t_{\text{diff}} = \left(\frac{2\kappa M_{\text{ej}}}{\beta c v_{\text{ej}}} \right)^{1/2}, \quad (5)$$

and includes a leakage parameter (Wang et al. 2015; Nicholl et al. 2017), not included in the original Arnett (1982) analytic expression, of the form:

$$A = \frac{3\kappa_{\gamma} M_{\text{ej}}}{4\pi v_{\text{ej}}^2}. \quad (6)$$

In this expression the parameter β has the typical value of 13.7 (Arnett 1982; Inserra et al. 2013), c is the speed of light, M_{ej} is the ejecta mass, v_{ej} is the characteristic ejecta velocity, κ is the optical opacity, and κ_{γ} is the opacity to high-energy photons. The leakage term, $(1 - e^{-At^{-2}})$, controls the fraction of high-energy photons thermalized by the SN ejecta (Wang et al. 2015; Nicholl et al. 2017). A large value of κ_{γ} implies a significant thermalization of the magnetar input energy at all times, while a small κ_{γ} value implies that a large fraction of the magnetar energy escapes at late times when the ejecta density drops.

In Fig. 9 we present the MOSFiT magnetar model fit result for SN 2002gh, where we fixed $z = 0.3653$ and the Galactic reddening to $E(B - V) = 0.0593$ mag in the fit. We do not allow MOSFiT to fit for host galaxy extinction or the gas column density parameters. Note that this fit describes reasonably well the light curve evolution, including the late V -band photometry, with the most significant

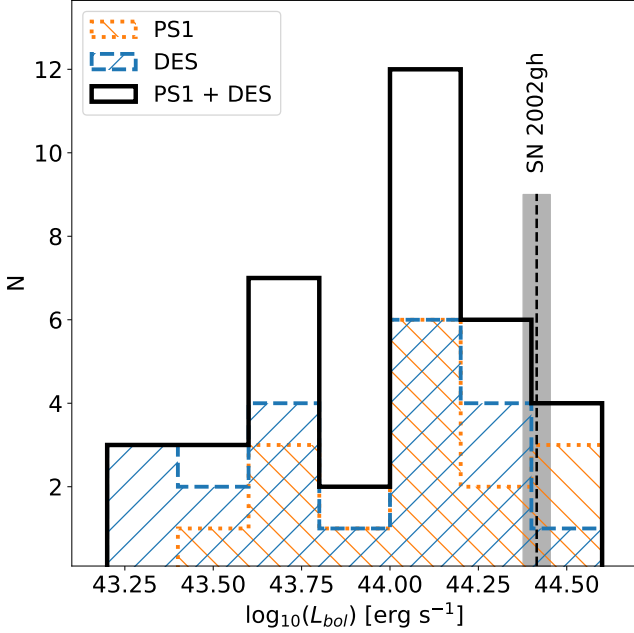


Figure 8. Observed maximum bolometric luminosity distribution for spectroscopically confirmed SLSNe from Pan-STARRS1 (Lunnan et al. 2018) and DES (Angus et al. 2019). This distribution includes peak bolometric luminosity for objects at $z > 1.2$, which are estimated using a heuristic method described in the Appendix. We mark with a black dashed line the maximum bolometric luminosity of SN 2002gh, confirming that it is among the most luminous SNe ever observed.

discrepancies in the B and I bands. We used additional information obtained from the analysis of SN 2002gh spectra presented in Section 3.5 to set restrictions on v_{ej} . In Section 3.5 below, we measure an ejecta expansion velocity between 9000 and 11,000 km s^{-1} over a rest-frame time of more than 60 days. Over this time interval we probed several layers of the SN ejecta, quantifying changes in the ejecta temperature, velocity, ionization state, and possibly in the ejecta composition. Therefore, it is expected that our estimate for the SN expansion velocity should be representative of the ejecta velocity, and hence v_{ej} should be close to the measured velocity. For this reason, a Gaussian prior on v_{ej} is employed, having a mean velocity of 10,000 km s^{-1} and a standard deviation of 1000 km s^{-1} . Additionally the following restriction $7,000 < v_{ej} < 16,000 \text{ km s}^{-1}$ is imposed. Without these restrictions a value of $v_{ej} \approx 5800 \text{ km s}^{-1}$ would be obtained with MOSFiT. This v_{ej} value represents 60% of the expansion velocity estimated from the minima of the spectral features in Section 3.5. The best MOSFiT values for SN 2002gh are summarized in Table 8. We highlight the huge ejecta mass of $M_{ej} \approx 25 M_{\odot}$ obtained by MOSFiT, and note that similar M_{ej} values are obtained regardless of the restrictions on v_{ej} .

In Fig. 10 is shown the analytic luminosity for the magnetar model using the MOSFiT parameters obtained for SN 2002gh, and compared with the bolometric light curve computed for SN 2002gh in the previous Section. There is an overall agreement between the two, but with the MOSFiT analytic light curve shifted by 0.10 to 0.15 dex to fainter luminosities than our estimated bolometric light curve. This shift is the result of differences in the methodologies employed to fit the modified blackbody model to the photometry and in the fitting procedure of the magnetar model itself. MOSFiT uses a Markov chain Monte Carlo (MCMC) fitter, to fit simultaneously for all the parameters in their model, including the photospheric velocity (v_{phot})

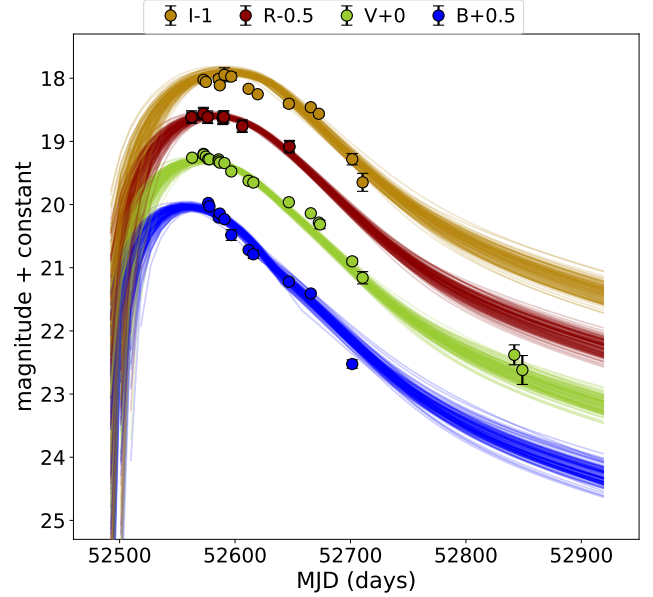


Figure 9. Magnetar model fit to SN 2002gh photometry using Nicholl et al. (2017) implementation in MOSFiT (Guillochon et al. 2018).

and the final plateau temperature (T_f) which determine the blackbody temperature and radius evolution. In our case the evolution of the temperature and radius are not parameterized but fitted at each epoch independently. Another difference is inclusion of the B band photometry in the fit, which in our case does not yield significant differences in the bolometric emission, but which under a different fitting methodology and a different implementation of the modified blackbody emission may be a source of systematic discrepancies. Additionally, the two methodologies use a slightly different version of the Galactic reddening law to account for the Galactic extinction, which may introduce a small but systematic difference in the same direction observed. The MOSFiT analytic luminosity light curve peaks about a week before the estimated epoch of the bolometric maximum, having a bolometric maximum luminosity of $1.5 \times 10^{44} \text{ erg s}^{-1}$ ($\log_{10}(L_{bol}) = 44.17$). This value represents 57.7% of the maximum luminosity estimated for SN 2002gh. Despite the constraints imposed on v_{ej} , MOSFiT still tends to converge to a low ejecta velocity.

Motivated by these small but apparent discrepancies, we decided to explore a wide parameter space and fit directly the bolometric light curve of SN 2002gh using consistently the Nicholl et al. (2017) magnetar model implementation. To simplify the model and to reduce the number of parameters to fit, we decided to fix the neutron star mass to $M_{NS} = 1.8 M_{\odot}$ and the ejecta velocity to $v_{ej} = 10,000 \text{ km s}^{-1}$. These values represent reasonable simplifying assumptions. Our strategy consists in assessing a wide range of parameters that reasonably reproduce the bolometric light curve of SN 2002gh. To this we used a grid over a large range in M_{ej} , B , P_{spin} , and κ and performed a least-squares minimization for t_{exp} , and κ_{γ} parameters to best fit the bolometric light curve of SN 2002gh. The ranges explored for M_{ej} , B , and P_{spin} are $0.63 \leq M_{ej} < 50.0 M_{\odot}$ with a logarithmic step of $\log_{10}(\Delta M_{ej}) = 0.1$, $0.1 \leq B < 12.5 \times 10^{14} \text{ G}$ with a logarithmic step of $\log_{10}(\Delta B) = 0.1$, $0.60 \leq P_{spin} < 7.25 \text{ ms}$ with a linear step of $\Delta P_{spin} = 0.20 \text{ ms}$, and $0.1 \leq \kappa \leq 0.2 \text{ cm}^2 \text{ gr}^{-1}$ with

a linear step of $\Delta\kappa = 0.025 \text{ cm}^2 \text{ gr}^{-1}$ respectively. We remark that our motivation here is to explore the magnetar parameter space and find the sets of values able to reproduce the bolometric light curve of SN 2002gh, not only the set that yields the best fit.

We computed the χ^2_ν for each set of parameters, and we used this value to find good fits that must also satisfy the energy balance requirement $E_K < E_{\text{mag}} - E_{\text{rad}} + E_\nu$ (see Nicholl et al. 2017). Where $E_K (= \frac{1}{2} M_{\text{ej}} v_{\text{ej}}^2)$ is the kinetic energy of the SN ejecta, E_{mag} is the magnetar rotational energy, E_{rad} is the energy radiated and $E_\nu \approx 10^{51} \text{ erg}$ is the canonical energy of a core-collapse explosion. Then, we selected the fits satisfying the energy balance and that also have $\chi^2_\nu < 20$. This χ^2_ν value was selected after visual inspection of the fits, providing a good threshold for reasonable fits.

Our exploration found two clearly distinct groups in the parameter space that reproduce the bolometric light curve of SN 2002gh. These two groups can be mainly distinguished by their ejecta mass and the need of a leakage parameter. The best magnetar parameters for these solutions are summarized in Table 8. We found that the best fits correspond to an ejecta mass in the range of 0.8 to $1.6 M_\odot$, κ_γ between 0.16 and $0.33 \text{ cm}^2 \text{ gr}^{-1}$, κ between 0.1 and $0.2 \text{ cm}^2 \text{ gr}^{-1}$, $P_{\text{spin}} = 3.4 \text{ ms}$, and $B = 0.50 \times 10^{14} \text{ G}$. These fits have a χ_ν between 1.96 and 1.99, and κ varies proportional to κ_γ and inversely proportional to the ejecta mass. The best fit is presented in the middle-panel of Fig. 10. The maximum luminosity of this model is $2.5 \times 10^{44} \text{ erg s}^{-1}$, consistent with our estimate, the rise time to maximum luminosity is 23.4 days, this corresponds to about 4 days in rest-frame before our estimated epoch of maximum luminosity. From about 65 days after the explosion, we see that in this case a noticeable fraction of the magnetar input energy leaks from the ejecta without being thermalized. This epoch corresponds to 37.5 days after our estimated epoch of bolometric maximum (MJD=52573.3). From about +70 days (90 days after the explosion), which corresponds to the phase of rapid decline, the energy leakage becomes even more evident in this model (see Fig. 10).

The second set of solutions is characterized by a huge ejecta mass between about 30 and $40 M_\odot$, having $\kappa_\gamma > 1.0 \text{ cm}^2 \text{ gr}^{-1}$. Note that the huge ejecta mass together with $\kappa_\gamma > 0.1 \text{ cm}^2 \text{ gr}^{-1}$, implies that the energy leakage is negligible and these solutions are equivalent to the case of no leakage. In these fits, the spin period is between 0.6 and 1.0 ms, the magnetic field is between 1.6 and $2.0 \times 10^{14} \text{ G}$, κ is between 0.175 and $0.2 \text{ cm}^2 \text{ gr}^{-1}$, and the best solutions for this case have $\chi_\nu \approx 2.8$. The rise time from the SN explosion to maximum luminosity is about 40 days, which corresponds to about 15 to 20 days before our estimated epoch of maximum luminosity. This model has a maximum luminosity of about $2.3 \times 10^{44} \text{ erg s}^{-1}$. The parameters for this case are in good agreement with the MOSFiT values, within the uncertainties (see 8). The agreement can be considered even better if the systematic differences between the two methodologies employed are considered. Hence, we consider the MOSFiT solution equivalent to our best bolometric fit without leakage.

3.4.2 Radioactive decay of ^{56}Ni

Here we explore the radioactive decay of ^{56}Ni as the possible power source for the light curve of SN 2002gh. The input energy from the ^{56}Ni radioactive decay (see Nadyozhin 1994) is:

$$F_{\text{Ni}}(t) = \left(6.45 \times 10^{43} e^{-t/\tau_{\text{Ni}}} + 1.45 \times 10^{43} e^{-t/\tau_{\text{Co}}} \right) \frac{M_{\text{Ni}}}{M_\odot} \text{ erg s}^{-1} \quad (7)$$

where $\tau_{\text{Ni}} = 8.8$ days and $\tau_{\text{Co}} = 111.3$ days are the e-folding decay times of ^{56}Ni and ^{56}Co , respectively. Assuming a rise time from the time of explosion to maximum luminosity of 20 days, and using the fact that at maximum light the ‘‘instant diffusion’’ equals the radioactivity input (Arnett 1979, 1982), from Eq. 7 we find that the minimum ^{56}Ni mass necessary to power the maximum luminosity of SN 2002gh is $M_{\text{Ni}} \approx 13 M_\odot$. For this case, and using the Arnett (1982) analytic solution, we require a total ejecta mass of $M_{\text{ej}} \approx 1.0 M_\odot$ to fit the light curve. In Fig. 11 the best fit to the bolometric light curve using radioactive decay of ^{56}Ni as energy source is presented. This is a non-physical solution as the total ejecta mass is smaller than the total ^{56}Ni mass. Increasing the rise time also increases the M_{Ni} necessary to fit the light curve, but we always find that $M_{\text{Ni}} > M_{\text{ej}}$. Since the total ejecta mass cannot be smaller than the ^{56}Ni mass required to power the SN luminosity, we conclude that SN 2002gh maximum luminosity cannot be powered by the ^{56}Ni radioactive decay. Although small amounts of ^{56}Ni (of about $\sim 0.1 M_\odot$) must be synthesized during the explosion, this energy source does not dominate the light curve evolution of SN 2002gh analysed here.

3.5 Line identification and spectral comparison

We present the spectral evolution of SN 2002gh in Fig. 4. The SN evolves smoothly from a very blue nearly featureless spectrum to a cool-photospheric phase dominated by moderately strong absorption lines. We divide, arbitrarily, the spectral evolution of SN 2002gh in four characteristic phases, namely, an early phase, followed by a cooling phase, a post-maximum phase, and a cool-photospheric phase. We analyse these phases in the following sub-sections, and we use for comparison SNe taken from the literature. The SNe used for comparison satisfy the following conditions: 1) have been well studied in the literature, thus we can use previous identifications to guide our line identification, and 2) show spectral features similar to SN 2002gh. These SNe are not necessarily representative of the whole diversity of the SLSN spectra (see e.g., Fig. 4 of Anderson et al. 2018; Quimby et al. 2018). The literature spectra were obtained from the WISeREP repository (Yaron & Gal-Yam 2012).

To distinguish the main ion(s) that contribute to form a spectral feature an approach similar to Gal-Yam (2019b) is followed. First, all permitted lines of several ions are considered (namely He I, C II, C III, O II, Mg II, Si II, Si III, Ca II, Ti III, Fe II, and Fe III). These lines compiled by the National Institute of Standards and Technology (NIST) cover the wavelength range from 2500 to 7000 Å. The relative intensities of the lines of a given ion are normalized by the maximum relative intensity of that ion over this wavelength range, then only lines with normalized relative intensities greater than 0.5 are considered for the line identification. However, a few exceptions are made for some C II, Fe II and Fe III lines. Since if we apply the criteria described before, we would leave out optical lines of these ions that can be distinguished in the spectra. This is because these ions have strong UV lines, with very large relative intensities making it impractical to apply this criteria in these few cases. Another exception to this criteria, is for ion lines that have been repeatedly associated with a spectral feature in the literature, so we decided to keep these lines in our line list for completeness.

In some cases, multiple strong lines of an ion are located close in wavelength ($< 100 \text{ Å}$), and due to the large ejecta expansion velocities (thousands of km s^{-1}), the lines appear blended contributing to form a single spectral feature. To simplify the line identification in these cases, these lines are represented as a single line having a mean wavelength computed using their relative intensities as weights for the

Table 8. Parameters of the magnetar model fits of SN 2002gh.

Magnetar parameters	M_{ej} (M_{\odot})	v_{ej} ($\times 10^3 \text{ km s}^{-1}$)	P_{spin} (m s)	B ($\times 10^{14} \text{ G}$)	κ ($\text{cm}^2 \text{ gr}^{-1}$)	κ_{γ} ($\text{cm}^2 \text{ gr}^{-1}$)	M_{NS} (M_{\odot})	χ_{ν}
MOSFiT	$25.1^{+5.1}_{-3.7}$	$7.8^{+0.6}_{-0.6}$	$1.2^{+0.2}_{-0.2}$	$1.9^{+3.8}_{-1.1}$	$0.17^{+0.02}_{-0.03}$	$6.0^{+125.8}_{-5.7}$	$1.7^{+0.2}_{-0.3}$	–
Bolometric fit no leakage	31.6	10.0^{\dagger}	1.0	1.6	0.200	∞	1.8^{\dagger}	2.79
Bolometric fit with leakage	1.6	10.0^{\dagger}	3.4	0.5	0.100	0.16	1.8^{\dagger}	1.96

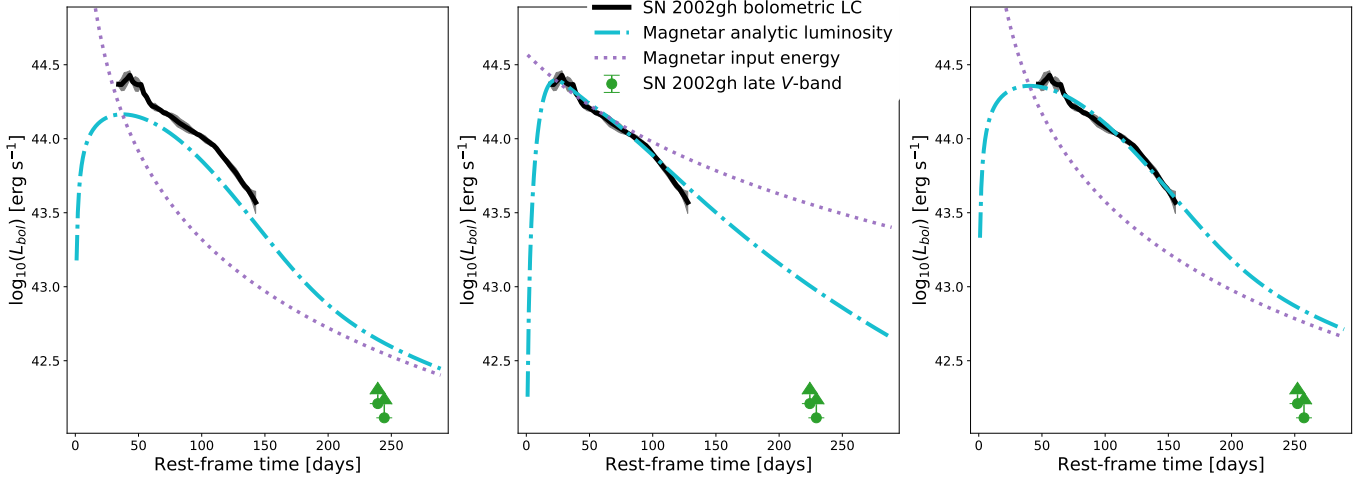
 † Fixed values.


Figure 10. Left panel: comparison between the MOSFiT analytic bolometric light curve (cyan dash-dotted line) and the observed bolometric light curve of SN 2002gh (black continuous). Note that MOSFiT fits the magnetar model to the photometry directly, and not to the observed bolometric light curve of SN 2002gh shown in this panel. In all the panels, the purple dotted line represents the magnetar input energy to the SN ejecta, and the green circles are the late time V-band photometry of SN 2002gh which provide a lower limit for the SN bolometric luminosity at this phase. Middle panel: best magnetar fit to the bolometric light curve of SN 2002gh using our grid exploration method and including leakage. Right panel: best magnetar fit to the bolometric light curve of SN 2002gh without energy leakage.

mean. The weighted means are computed over wavelength intervals of 30 to 100 Å. An example of this methodology is the H&K Ca II doublet $\lambda\lambda$ 3933.66, 3968.47, which in the SN spectra yield a blended feature with a weighted mean wavelength of 3950.29 Å.

With these ion line lists in hand, and in combination with line identification and radiative transfer models of SLSNe from the literature (e.g., Mazzali et al. 2016; Quimby et al. 2018; Dessart 2019; Gal-Yam 2019b) we associate these ion lines to spectral features. We also considered Hatano et al. (1999) synthetic spectra computation for C/O-rich and carbon-burned compositions to guide our line identification.

3.5.1 Early phase

In Fig. 12, the spectrum of SN 2002gh is compared with other SLSNe at a similar spectral phase. These spectra are characterized by a very blue continuum, well described by a blackbody, and by the presence of the distinctive O II lines in the spectrum in the wavelength range from 3500 to 5000 Å (see Quimby et al. 2018). O II features are the hallmark of hydrogen-poor SLSNe at an early phase, and these lines are extremely rare in other CCSNe as it requires oxygen to be excited to a high energy level (Mazzali et al. 2016). The spectra of SN 2002gh from -8 to +2 days show the distinctive signatures of this phase.

As shown in Fig. 12, the expansion velocity of SN 2002gh measured from the minimum of the O II is about 10,000 km s⁻¹ and its photospheric temperature is about 14,000 K (see Fig. 6). The strong spectral feature at 2830 Å has been associated with Ti III for iPTF13ajg by Mazzali et al. (2016). In Fig. 12 we confirm the possible contribution of Ti III, and we add the likely contribution from Mg II to this feature, both ions at an expansion velocity of about 10,000 km s⁻¹. In the spectra of SN 2002gh the blue side of this feature is affected by the Mg II $\lambda\lambda$ 2796, 2803 doublet absorption from the host galaxy, which is indicated with a pink tick mark in Fig. 12. After a careful inspection, the minimum of this absorption feature seems to be redwards of the host galaxy absorption, and favours Mg II as the dominant ion for this feature in SN 2002gh.

On the blue side of the iPTF13ajg spectrum, the strong 2670 Å feature has usually been associated to Mg II or to a combination of Mg II and C II lines. However, unless a significantly different expansion velocity is assumed, as can be seen in Fig. 12, the Mg II λ 2660.79 and λ 2797.34 lines lie on the blue and on the red side of this feature, respectively. The strong C II λ 2837.05 is located too far to the red to be considered the main contributor to this feature, as has been also noted by Quimby et al. (2018). There is a weaker C II λ 2741.28 line that is located at the right wavelength, but since no signature of the stronger C II λ 2837.05 line is detected, it makes it unlikely that C II λ 2741.28 line is the dominant ion producing such a strong spectral

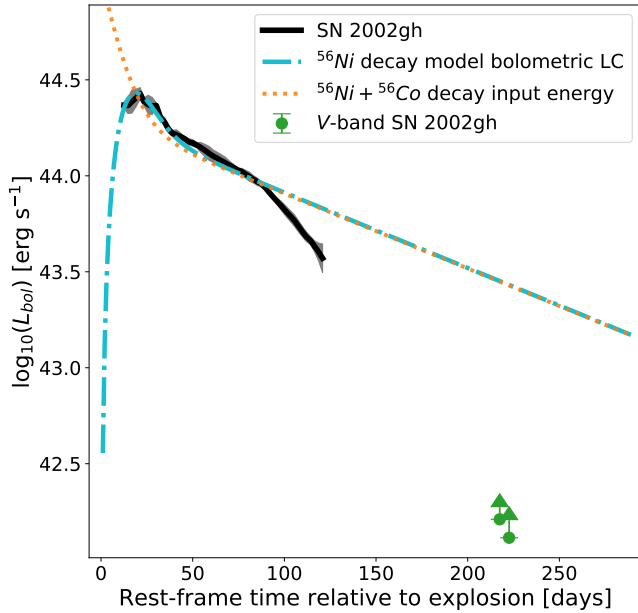


Figure 11. Bolometric light curve fit to SN 2002gh using the Arnett (1982) analytic approximation and the radioactive decay of ^{56}Ni (Eq. 7) as the power source. The parameters of the best fit model are $\tau_{\text{rise}} = 20.7$ days, $M_{\text{ej}} = 1.1 M_{\odot}$, $M_{\text{Ni}} = 13.9 M_{\odot}$, $v_{\text{ej}} = 10,000 \text{ km s}^{-1}$ and $\kappa = 0.2 \text{ cm}^2 \text{ gr}^{-1}$. This model illustrates that the light curve of SN 2002gh follows an evolution “consistent” with the ^{56}Ni decay until about 70-80 days post maximum. However, the best fit obtained with the ^{56}Ni decay model is non-physical as $M_{\text{Ni}} > M_{\text{ej}}$, thus we rule out the ^{56}Ni decay as the main power source for SN 2002gh.

feature. An alternative possibility is that this feature may have a significant contribution from several strong Fe II lines with a weighted mean wavelength of 2747.94 \AA , as illustrated in Fig. 12. These are the strongest set of Fe II lines over the whole wavelength range considered here, and even a small amount of Fe II may produce a feature at this location, so we consider it very likely that Fe II contributes to form this feature in addition to Mg II and C II. We notice that a strong absorption feature at this wavelength, due to the combination of Fe II and Mg II lines, has been recognized before in the UV spectra of SN 2011fe (Mazzali et al. 2014). Although SN 2011fe is a SN Ia, Fe II and Mg II are also present in hydrogen-poor SLSNe and the spectral features produced by these ions should be similar, giving support to this identification.

We identify three absorption features in LSQ14bdq as tentative Fe III lines, in the region between 3100 \AA and 3500 \AA . We further identify these features in the early spectra of iPTF13ajg (see also Fig. 13). However, these features are not clearly present in SN 2002gh. We note that other strong Fe III lines have wavelengths coincident with O II features (see Fig. 13), furthermore the C III $\lambda 4649.97$ feature is coincident and may contribute to the O II A feature at this phase.

We find that the early phase spectra of SN 2002gh show similar features to the early spectra of LSQ14bdq (Nicholl et al. 2015), and also to the early and near maximum spectra of iPTF13ajg (Vreeswijk et al. 2014).

3.5.2 Cooling phase

This phase begins at a few days after maximum and ends between 10 and 20 days past maximum, and it is characterized by a decrease

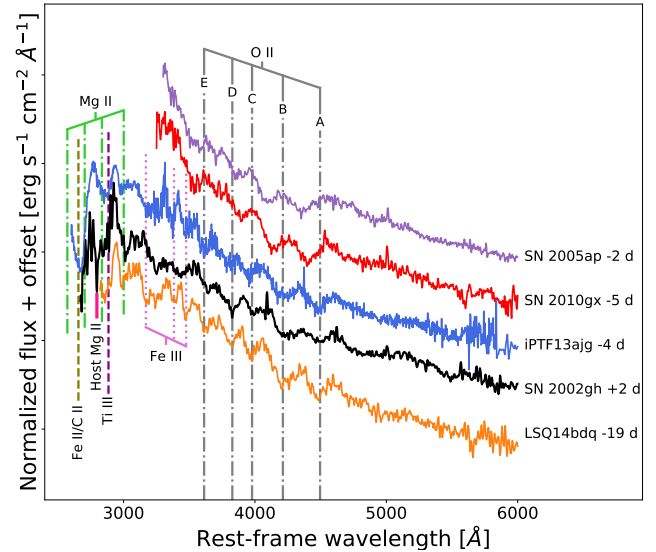


Figure 12. Early phase spectra characterized by O II spectral features in the $3500\text{-}5000 \text{ \AA}$ range. The vertical dot-dashed lines represent the effective wavelength for the A, B, C, D, and E O II spectral features identified by Quimby et al. (2018) at an expansion velocity of $10,000 \text{ km s}^{-1}$. We identify and mark other ions with vertical lines such as the Ti III $\lambda 2984.747$ line identified by Mazzali et al. (2016), C II, Mg II, Fe II and Fe III lines at the same expansion velocity of $10,000 \text{ km s}^{-1}$. We mark the host galaxy Mg II $\lambda\lambda 2796, 2803$ doublet absorption feature with a pink tick. For comparison, we present the spectra of SN 2005ap (Quimby et al. 2007), SN 2010gx (Pastorello et al. 2010), iPTF13ajg (Vreeswijk et al. 2014), and LSQ14bdq (Nicholl et al. 2015).

in the strength of the characteristic O II lines, until they disappear at the end of this phase. This is a consequence of the decrease in the ionization state of the SN ejecta after maximum light. However, the SN ejecta remains hot enough for Fe III features to take the place of O II features, while the latter decrease their strength significantly. This evolution is reflected in: 1) O II A and E features fade quicker than other O II features after maximum, 2) the O II C and D features, which are coincident with Fe III lines, remain visible in the SN spectra for longer time than A and E features, and 3) in the meantime, the O II B feature which is blended with Fe III, Fe II and Mg II lines, increases its strength and quickly shifts to the red. At this phase, this feature exhibits a distinctive double absorption due to Fe III in the blue and to Mg II in the red. In Fig. 13 we illustrate the Fe III lines and the Mg II $\lambda 4446.31$ feature at an expansion velocity of 9500 km s^{-1} in the region previously dominated by O II lines. These two minima can be clearly distinguished in SN 2015bn and SN 2010gx. Contemporary to this, Fe II lines give shape to the broad spectral feature in the region between $4500\text{-}5250 \text{ \AA}$ (see Fig. 13). We note that the spectrum of SN 2015bn is shifted by 2500 km s^{-1} to the blue in Fig 13, to match with the spectral features of SN 2002gh.

As before, the Fe III absorption features are tentatively distinguished in the spectra of iPTF13ajg and SN 2015bn in the region between 3100 \AA and 3500 \AA . However, the identification of these features is less clear in SN 2002gh. We associate the feature at 3000 \AA with Mg II in SN 2002gh and iPTF13ajg. The spectral feature at 2830 \AA has now shifted blueward in these SNe, now in a better agreement with the Mg II line rather than with the Ti III line, suggesting a decrease in the contribution of the latter ion to this feature. We associate the strong 2670 \AA feature with Fe II and Mg II lines, and note that the minimum of this feature is bluer in SN 2002gh. Possible explanations for this are; 1) a higher expansion velocity of the

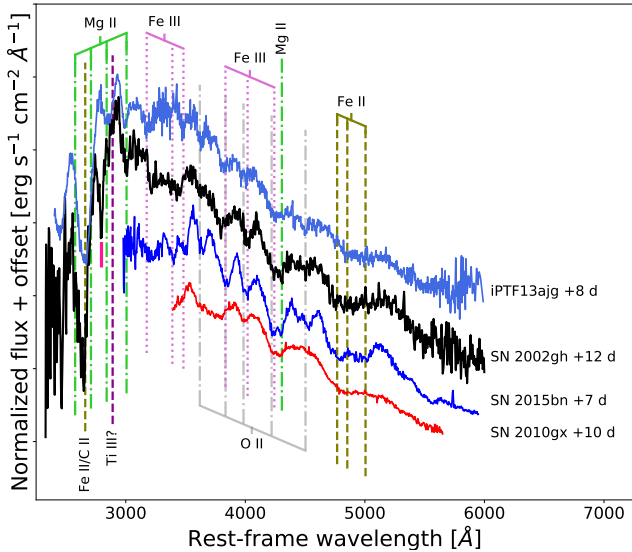


Figure 13. Post-maximum cooling phase comparison. The lines of several ions are marked and identified with vertical lines at an expansion velocity of 9500 km s^{-1} . For comparison, we present spectra of SN 2010gx, iPTF13ajg, and SN 2015bn (Nicholl et al. 2016a). In addition to the correction by the host galaxy recession velocity, the spectrum of SN 2015bn has been shifted to the blue by 2500 km s^{-1} to match the SN 2002gh spectrum at this phase. We highlight the Mg II $\lambda\lambda 2796, 2803$ doublet absorption from the SN 2002gh host galaxy with a pink tick.

line producing this feature in SN 2002gh, 2) a contribution from an unidentified ion not present in the iPTF13ajg spectrum or 3) host galaxy absorption lines shifting the line to the blue as in the case of the Mg II host galaxy absorption line that ‘shifts’ the 2830 Å feature to the blue. Several strong Fe II lines on the blue side of this feature at the host galaxy rest-frame can be potentially identified, providing support to the latter possibility.

The spectra of SN 2002gh from +9 to +12 days are representative of this phase. The average decrease of the SN 2002gh ejecta temperature is about 340 K per day, with an approximate ejecta temperature within the range of about 13,500 to 11,000 K in the course of this phase. We find that the spectra of SN 2002gh at this phase are similar to iPTF13ajg and SN 2015bn (after shifting the latter spectrum to the blue in Fig. 13).

3.5.3 Post-maximum phase

The beginning of this phase can be defined as when high-ionization lines such as O II and Fe III lines vanish, and the dominant spectral features are produced by Fe II, Mg II and other IME’s. These changes make hydrogen-poor SLSNe exhibit spectral features similar to SNe Ic and Ic-BL at an early phase (Fig. 14), but the spectral features of SLSNe are shallower and have a bluer continuum.

At this phase, we distinguish the 3800 Å feature produced by Mg II and the H&K Ca II lines, the 4315 Å feature produced by Mg II and Fe II lines and the broad feature between 4500–5250 Å produced mainly by Fe II lines, but with contributions from other IME’s such as Mg II. Notably, the 4315 Å feature has evolved from being produced by the O II B feature, then produced by a combination of Fe III, Fe II and Mg II with a distinctive double absorption feature such as in SN 2015bn and SN 2010gx, to a single absorption produced by Mg II and Fe II at this phase. Note that there is an Fe II line close in wavelength to the Mg II line in this feature, which we do not mark in

Fig. 14 to avoid crowding. Additional Fe II lines to the blue and to the red also shape this feature.

At the UV wavelengths, the spectral features at 2670 Å and 2830 Å remain, and Fe II and Mg II are the main suspects to explain these features. At this phase, for first time, the Ca II features are distinguished in this wavelength range, and they contribute to the spectral features at 3080 Å and 3800 Å blended with Mg II lines, and to the 3610 Å feature in SN 2015bn (see Fig. 14). The three strongest Ca II features over this range have weighted mean wavelengths of 3172.79 Å, 3722.35 Å and 3950.29 Å. The spectra of SN 2002gh at +24 and +28 days are representative of this phase, where the ejecta expansion velocity is about 9000 km s^{-1} and $T_{\text{bb}} \sim 10,500 \text{ K}$.

3.5.4 Cool-photospheric phase

As the ejecta temperature decreases the resemblance of SLSNe to SNe Ic and Ic-BL becomes more evident, the pseudo-continuum becomes redder and the strengths of the lines increase, as can be seen in Fig. 14. When the ejecta temperature of SLSNe is about or below 10,000 K the strength of the 4315 Å feature in SLSNe becomes similar to SNe Ic. This is the case of SN 2002gh from about +50 days, when the ejecta temperature is about 9500 K and the ejecta expansion velocity is slightly below 9000 km s^{-1} .

In Fig. 14, we notice that while the 4315 Å feature in SLSNe has reached a strength roughly similar as in the Ic SN 1994I, the spectral feature between 4500–5250 Å, although stronger than in previous phases, is shallower than in SNe Ic and Ic-BL. The UV emission has decreased due to the decline of the ejecta temperature and due to an increase of absorption from IME’s and Fe II lines. The spectral features at 2670 Å and 2830 Å remain. The SLSN emission it is now slowly evolving towards the pseudo-nebular phase.

4 DISCUSSION AND CONCLUSIONS

We have presented and analysed excellent quality observations of SN 2002gh obtained as part of the CATS project. SN 2002gh is at a redshift of $z = 0.3653 \pm 0.0005$, it was the second SLSN-I discovered after SN 1999as, and its true nature remained unnoticed for two decades. The multi-band observations presented here for SN 2002gh cover nearly 300 days of the SN evolution, with the well sampled spectral sequence comprising more than 80 days. These observations make of SN 2002gh a perfect object for a detailed study, such as the one presented here, placing this SLSN among the best observed and studied to date.

In Section 3.1 we identified the potential SN 2002gh’s host galaxy in deep DECam images. The potential host is a faint dwarf galaxy, presumably having low metallicity as is common for a SLSN-I hosts (Lunnan et al. 2014; Leloudas et al. 2015; Perley et al. 2016; Schulze et al. 2018), located $0''.13$ south-east from the SN location corresponding to a projected distance of 0.67 kpc, at the SN redshift. The host galaxy candidate shows irregular morphology and multiple emission peaks. The multi-peak morphology could be tracing regions of strong star-formation within the irregular host or could be interpreted as a system of dwarf galaxies in a merging process. Recently, Ørum et al. (2020) found that hydrogen-poor SLSN host galaxies are often part of interacting systems, with $\sim 50\%$ having at least one major companion within 5 kpc. They interpreted this as SLSN-I being the result of a recent burst of star formation, possibly triggered by galaxy interaction. Future confirmation that the SN 2002gh’s host galaxy is part of a system of dwarf galaxies in a merging process, would provide further support to the Ørum et al. (2020) hypothesis.

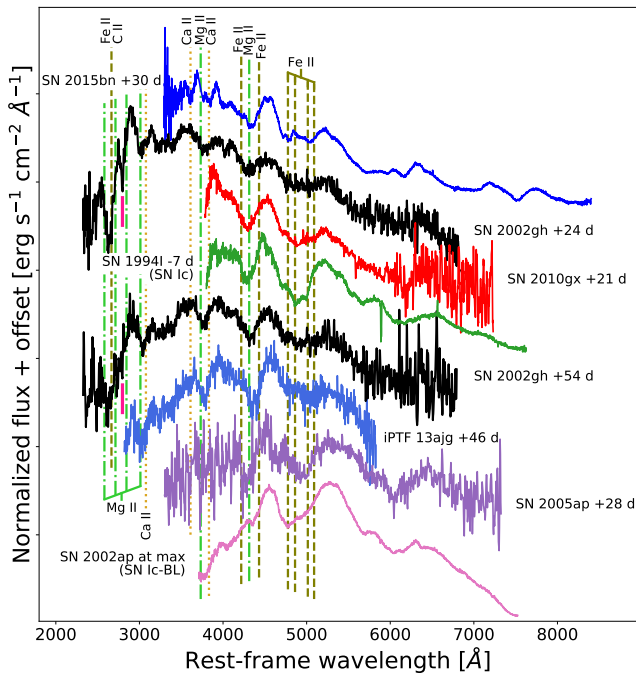


Figure 14. Post-maximum and cool-photospheric phase comparison. We mark and identify the lines of several ions with vertical lines at an expansion velocity of 9000 km s^{-1} . For comparison, we present the spectra of Type Ic SN 1994I and Type Ic-BL SN 2002ap (Modjaz et al. 2014), and the hydrogen-poor SLSN 2005ap, SN 2010gx, iPTF13ajg, and SN 2015bn. As in Fig. 13, the spectrum of SN 2015bn has been shifted to the blue by 2500 km s^{-1} . As before, we highlight the Mg II $\lambda\lambda$ 2796, 2803 doublet host galaxy absorption in SN 2002gh spectra with a pink tick.

Further deep spectroscopy of the host galaxy candidate is required for a solid association with the SN and to understand the nature of the multi-peak morphology.

In Sections 3.2 and 3.3 we characterized the light curves of SN 2002gh and computed its bolometric light curve assuming that the SN emission can be well described by a modified blackbody. We distinguished four phases in the light curves of SN 2002gh. The first phase associated with the maximum light and the immediate decline from maximum, a second phase from about two weeks to $\approx +70$ days post maximum, which is characterized by a bolometric decline rate roughly consistent with the decline rate expected for a SN powered by ^{56}Co decay. A third phase, from about +70 days to ≈ 100 days, characterized by a faster decline rate in all bands. The last phase comprises the last three photometric observations in the V-band, with a gap of nearly a hundred days between the first and the last two points. We find that the average decline rate value over this phase is reduced compared to the decline rate of the previous phase, indicating a possible flattening of the light curve at about 200 days after maximum.

In Section 3.3 we find that the maximum bolometric luminosity of SN 2002gh is $2.6 \pm 0.2 \times 10^{44} \text{ erg s}^{-1}$ ($\log_{10}(L_{\text{bol}}^{\text{peak}}) \approx 44.4$). Our study presents a large set of bolometric light curves for 28 SLSNe-I, 11 from Pan-STARRS1 (Lunnan et al. 2018) and 17 from DES (Angus et al. 2019), showing the large diversity in shapes, including the presence of pre- and post-maximum bumps, and a large range in maximum luminosities from $\log_{10}(L_{\text{bol}}) \approx 43.2$ to $\log_{10}(L_{\text{bol}}) < 44.6$. A comparison of the bolometric light curve of SN 2002gh with these objects shows that SN 2002gh is the brightest in this sample. Comparing the estimated maximum bolometric luminosity for a total

sample of 37 SLSNe-I, 16 from Pan-STARRS1 and 21 from DES, we show that SN 2002gh is among the most luminous SNe ever observed.

In Section 3.4 we study the magnetar model and the radioactive decay of ^{56}Ni as power sources of SN 2002gh. We rule out the radioactive decay of ^{56}Ni as the main power source for the light curve of SN 2002gh, finding that a minimum of $\approx 13 M_{\odot}$ of ^{56}Ni are needed to power the peak luminosity of SN 2002gh, an unrealistically large value. Moreover, the best analytic fitting to the bolometric light curve always requires a total ejecta mass below the ^{56}Ni mass, which is a non-physical solution, thus ruling out the radioactive decay of ^{56}Ni as the main power source for SN 2002gh. Although some amount of ^{56}Ni must be synthesized during the SN explosion.

We found that the spin down of a magnetar can explain the huge maximum luminosity observed in SN 2002gh. Fitting an analytic magnetar model to the observed bolometric light curve of SN 2002gh we found two alternative solutions. The first solution, requires significant leakage of the magnetar input energy (see Fig. 10), of which the rapid decline observed in the third phase of the SN light curves could be a signature. We found that the best fit to the bolometric light curve is for M_{ej} between 0.8 and $1.6 M_{\odot}$, $P_{\text{spin}} = 3.4 \text{ ms}$, and $B = 5 \times 10^{13} \text{ G}$. The alternative magnetar model does not require power leakage, and it is characterized by a huge ejecta mass of 25 to $40 M_{\odot}$, a fast spin period of P_{spin} between 0.6 and 1.2 ms , and B between 1.6 and $2.0 \times 10^{14} \text{ G}$.

SN 2002gh lacks signatures of hydrogen or helium mixed in the SN ejecta, therefore it must have lost all its hydrogen and a significant part of its helium envelope through winds, but also through binary interaction, since half or more of all massive stars are found in binary systems. Using equations 13 and 14 of Woosley (2019) for evolution models of massive helium stars of solar metallicity, and assuming a final mass (M_{fin}) before the explosion between 2.6 and $3.4 M_{\odot}$ and of $30 M_{\odot}$ for the first and second case of the magnetar model, respectively, we estimate a zero-age main-sequence mass between 16 and $19 M_{\odot}$ for the first case and of about $135 M_{\odot}$ for the second case. The latter case would place the progenitor star of SN 2002gh among the most massive stars observed to explode as a SN.

We do not find any evidence for ejecta-CSM interaction. The spectral features of SN 2002gh are typical of a non-interacting SN, resembling non-interacting stripped envelope core-collapse SNe from about +24 days to the last spectrum at about +54 days (see Fig. 14) relative to the bolometric maximum. However, we cannot rule out completely the case of ejecta-CSM interaction in SN 2002gh, but we can place some constraints on the potential CSM composition, such as the CSM must be hydrogen and helium poor. We also note that the magnetar model can explain reasonably well the observations of SN 2002gh without the need to invoke the additional power contribution from the ejecta-CSM interaction.

In Section 3.5 we study the spectral evolution of SN 2002gh. In this section we divide, arbitrarily, the spectral evolution of SN 2002gh in four characteristic phases, namely, an early phase, followed by a cooling phase, a post-maximum phase, and a cool-photospheric phase. We identify several ions at an expansion velocity decreasing from $11,000$ in the early phase to 9000 km s^{-1} in the later phases. We compare the spectra of SN 2002gh with well observed hydrogen-poor SLSNe and stripped envelope core-collapse SNe from the literature. We found that its spectral evolution is typical of an object of this class displaying O II lines before and close to maximum light, following a cooling phase, where the Fe II lines become prominent features. After about +24 days the SN starts to resemble to Type Ic SN 1994I or to Type Ic-BL SN 2002ap at an early phase. Among SLSNe, SN 2002gh

shows significant spectroscopic similarity to iPTF13ajg, also a very bright object among this SN class (Vreeswijk et al. 2014).

ACKNOWLEDGMENTS

We thank to Matt Nicholl for his prompt and helpful response about MOSFiT inquiries. This research draws upon DECam data as distributed by the NOIRLab Astro Data Archive. NOIRLab is managed by the Association of Universities for Research in Astronomy (AURA) under a cooperative agreement with the National Science Foundation. MDS is supported by grants from the VILLUM FONDEN (grant number 28021) and the Independent Research Fund Denmark (IRFD; 8021-00170B).

This project used data obtained with the Dark Energy Camera (DECam), which was constructed by the Dark Energy Survey (DES) collaboration. Funding for the DES Projects has been provided by the US Department of Energy, the US National Science Foundation, the Ministry of Science and Education of Spain, the Science and Technology Facilities Council of the United Kingdom, the Higher Education Funding Council for England, the National Center for Supercomputing Applications at the University of Illinois at Urbana-Champaign, the Kavli Institute for Cosmological Physics at the University of Chicago, Center for Cosmology and Astro-Particle Physics at the Ohio State University, the Mitchell Institute for Fundamental Physics and Astronomy at Texas A&M University, Financiadora de Estudos e Projetos, Fundação Carlos Chagas Filho de Amparo à Pesquisa do Estado do Rio de Janeiro, Conselho Nacional de Desenvolvimento Científico e Tecnológico and the Ministério da Ciência, Tecnologia e Inovação, the Deutsche Forschungsgemeinschaft and the Collaborating Institutions in the Dark Energy Survey.

The Collaborating Institutions are Argonne National Laboratory, the University of California at Santa Cruz, the University of Cambridge, Centro de Investigaciones Energéticas, Medioambientales y Tecnológicas–Madrid, the University of Chicago, University College London, the DES-Brazil Consortium, the University of Edinburgh, the Eidgenössische Technische Hochschule (ETH) Zürich, Fermi National Accelerator Laboratory, the University of Illinois at Urbana-Champaign, the Institut de Ciències de l’Espai (IEEC/CSIC), the Institut de Física d’Altes Energies, Lawrence Berkeley National Laboratory, the Ludwig-Maximilians Universität München and the associated Excellence Cluster Universe, the University of Michigan, NSF’s NOIRLab, the University of Nottingham, the Ohio State University, the OzDES Membership Consortium, the University of Pennsylvania, the University of Portsmouth, SLAC National Accelerator Laboratory, Stanford University, the University of Sussex, and Texas A&M University.

Based on observations at Cerro Tololo Inter-American Observatory, a program of NOIRLab (NOIRLab Proposal ID #2014B-0404; PIs: David Schlegel and Arjun Dey and NOIRLab Proposal ID #2019A-0305; PI: Alex Drlica-Wagner), which is managed by the Association of Universities for Research in Astronomy (AURA) under a cooperative agreement with the National Science Foundation.

DATA AVAILABILITY

The photometric data of SN 2002gh is available in the article and the spectra are available on request to the corresponding author and also available from the WISEREP archive² (Yaron & Gal-Yam 2012).

² <http://wiserep.weizmann.ac.il/>

REFERENCES

- Amorín R., et al., 2014, *A&A*, 568, L8
 Amorín R., et al., 2015, *A&A*, 578, A105
 Anderson J. P., et al., 2018, *A&A*, 620, A67
 Angus C. R., Levan A. J., Perley D. A., Tanvir N. R., Lyman J. D., Stanway E. R., Fruchter A. S., 2016, *MNRAS*, 458, 84
 Angus C. R., et al., 2019, *MNRAS*, 487, 2215
 Arnett W. D., 1979, *ApJ*, 230, L37
 Arnett W. D., 1982, *ApJ*, 253, 785
 Atek H., et al., 2011, *ApJ*, 743, 121
 Barbary K., et al., 2009, *ApJ*, 690, 1358
 Barkat Z., Rakavy G., Sack N., 1967, *Phys. Rev. Lett.*, 18, 379
 Bertin E., Arnouts S., 1996, *A&AS*, 117, 393
 Bertin E., Mellier Y., Radovich M., Missonnier G., Didelon P., Morin B., 2002, in Bohlender D. A., Durand D., Handley T. H., eds, *Astronomical Society of the Pacific Conference Series Vol. 281, Astronomical Data Analysis Software and Systems XI*. p. 228
 Bessell M. S., 1990, *PASP*, 102, 1181
 Bessell M. S., 2005, *ARA&A*, 43, 293
 Bessell M. S., Castelli F., Plez B., 1998, *A&A*, 333, 231
 Cardamone C., et al., 2009, *MNRAS*, 399, 1191
 Cardelli J. A., Clayton G. C., Mathis J. S., 1989, *ApJ*, 345, 245
 Cartier R., et al., 2014, *ApJ*, 789, 89
 De Cia A., et al., 2018, *ApJ*, 860, 100
 Dessart L., 2018, *A&A*, 610, L10
 Dessart L., 2019, *A&A*, 621, A141
 Dessart L., Hillier D. J., Waldman R., Livne E., Blondin S., 2012, *MNRAS*, 426, L76
 Filippenko A. V., 1997, *ARA&A*, 35, 309
 Flaugher B., et al., 2015, *AJ*, 150, 150
 Fukugita M., Ichikawa T., Gunn J. E., Doi M., Shimasaku K., Schneider D. P., 1996, *AJ*, 111, 1748
 Gal-Yam A., 2019a, *ARA&A*, 57, 305
 Gal-Yam A., 2019b, *ApJ*, 882, 102
 Gal-Yam A., et al., 2009, *Nature*, 462, 624
 Gezari S., et al., 2009, *ApJ*, 690, 1313
 Grayling M., et al., 2021, arXiv e-prints, p. arXiv:2103.14669
 Guillochon J., Nicholl M., Villar V. A., Mockler B., Narayan G., Mandel K. S., Berger E., Williams P. K. G., 2018, *ApJS*, 236, 6
 Hamuy M., et al., 2003, *Nature*, 424, 651
 Hamuy M., et al., 2006, *PASP*, 118, 2
 Hamuy M., et al., 2009, *ApJ*, 703, 1612
 Hatano K., Branch D., Fisher A., Millard J., Baron E., 1999, *ApJS*, 121, 233
 Heger A., Woosley S. E., 2002, *ApJ*, 567, 532
 Inserra C., et al., 2013, *ApJ*, 770, 128
 Inserra C., et al., 2018, *MNRAS*, 475, 1046
 Jerkstrand A., Smartt S. J., Heger A., 2016, *MNRAS*, 455, 3207
 Jerkstrand A., et al., 2017, *ApJ*, 835, 13
 Jerkstrand A., Maeda K., Kawabata K. S., 2020, *Science*, 367, 415
 Kasen D., Bildsten L., 2010, *ApJ*, 717, 245
 Knop R., et al., 1999, *IAU Circ.*, 7128, 1
 Leloudas G., et al., 2015, *MNRAS*, 449, 917
 Liu Y.-Q., Modjaz M., Bianco F. B., 2017, *ApJ*, 845, 85
 Lunnan R., et al., 2014, *ApJ*, 787, 138
 Lunnan R., et al., 2015, *ApJ*, 804, 90
 Lunnan R., et al., 2018, *ApJ*, 852, 81
 Maeda K., et al., 2007, *ApJ*, 666, 1069
 Mazzali P. A., et al., 2014, *MNRAS*, 439, 1959
 Mazzali P. A., Sullivan M., Pian E., Greiner J., Kann D. A., 2016, *MNRAS*, 458, 3455
 Mazzali P. A., Moriya T. J., Tanaka M., Woosley S. E., 2019, *MNRAS*, 484, 3451
 Milisavljevic D., et al., 2013, *ApJ*, 770, L38
 Miller A. A., et al., 2009, *ApJ*, 690, 1303
 Modjaz M., et al., 2014, *AJ*, 147, 99
 Moriya T. J., Sorokina E. I., Chevalier R. A., 2018, *Space Sci. Rev.*, 214, 59
 Nadyozhin D. K., 1994, *ApJS*, 92, 527

- Neill J. D., et al., 2011, *ApJ*, 727, 15
 Nicholl M., et al., 2015, *ApJ*, 807, L18
 Nicholl M., et al., 2016a, *ApJ*, 826, 39
 Nicholl M., et al., 2016b, *ApJ*, 828, L18
 Nicholl M., Guillochon J., Berger E., 2017, *ApJ*, 850, 55
 Nicholl M., Berger E., Blanchard P. K., Gomez S., Chornock R., 2019, *ApJ*, 871, 102
 Ofek E. O., et al., 2007, *ApJ*, 659, L13
 Ørum S. V., Ivens D. L., Strandberg P., Leloudas G., Man A. W. S., Schulze S., 2020, *A&A*, 643, A47
 Pastorello A., et al., 2010, *ApJ*, 724, L16
 Pedregosa F., et al., 2011, *Journal of Machine Learning Research*, 12, 2825
 Perley D. A., et al., 2016, *ApJ*, 830, 13
 Quimby R. M., Aldering G., Wheeler J. C., Höflich P., Akerlof C. W., Rykoff E. S., 2007, *ApJ*, 668, L99
 Quimby R. M., et al., 2011, *Nature*, 474, 487
 Quimby R. M., Yuan F., Akerlof C., Wheeler J. C., 2013, *MNRAS*, 431, 912
 Quimby R. M., et al., 2018, *ApJ*, 855, 2
 Rakavy G., Shaviv G., 1967, *ApJ*, 148, 803
 Schlafly E. F., Finkbeiner D. P., 2011, *ApJ*, 737, 103
 Schlegel E. M., 1990, *MNRAS*, 244, 269
 Schulze S., et al., 2018, *MNRAS*, 473, 1258
 Smith N., et al., 2007, *ApJ*, 666, 1116
 Smith M., et al., 2016, *ApJ*, 818, L8
 Tonry J. L., et al., 2012, *ApJ*, 750, 99
 Vreeswijk P. M., et al., 2014, *ApJ*, 797, 24
 Wang S. Q., Wang L. J., Dai Z. G., Wu X. F., 2015, *ApJ*, 799, 107
 Wood-Vasey W. M., Aldering G., Nugent P., Rudas R., 2002, *IAU Circ.*, 7990
 Woosley S. E., 2010, *ApJ*, 719, L204
 Woosley S. E., 2019, *ApJ*, 878, 49
 Woosley S. E., Blinnikov S., Heger A., 2007, *Nature*, 450, 390
 Yan L., et al., 2015, *ApJ*, 814, 108
 Yan L., et al., 2017, *ApJ*, 848, 6
 Yaron O., Gal-Yam A., 2012, *PASP*, 124, 668

APPENDIX A: BOLOMETRIC LIGHT CURVES

We constructed bolometric light curves from Pan-STARRS1 (PS1; Lunnan et al. 2018) and DES (Angus et al. 2019) SLSNe following a procedure almost identical to the one used for SN 2002gh. First we interpolated their light curves using the PYTHON Gaussian process module implemented in SCIKIT-LEARN (Pedregosa et al. 2011). The PS1 dataset is composed of observations in *grizy* reaching a depth slightly fainter than ~ 23.3 mag in *griz* and ~ 22 in *y*-band. Only a handful of objects have *y*-band photometry, usually more noisy than on the other filters. DES present a homogeneous set of photometry in *griz* passbands to a depth of ~ 24 mag, obtained with the Dark Energy Camera (Flaugher et al. 2015) which is mounted on the 4 meter Blanco telescope at Cerro Tololo in Chile. In figures A1 and A2 we present two examples of the light curves interpolation, for PS1-1lap (Fig. A1) and for DES14X2byo (Fig. A2). One of the advantages of using Gaussian process interpolation is its flexibility, providing an excellent fit to the SLSNe light curves, as can be observed in these examples. At the same time, this approach provides a robust estimate for the uncertainty in the interpolation. Using this approach we obtained an homogeneous set of 37 multi-band interpolated light curves with their respective uncertainties, the latter point is key for the determination of the uncertainties in blackbody parameters and in our bolometric light curves.

To model the SLSN emission we fitted the interpolated light curves corrected by Galactic reddening using a modified blackbody SED. To correct the light curves by Galactic reddening we used $E(B - V)$ values from Schlafly & Finkbeiner (2011) and the Cardelli et al. (1989) reddening law with $R_V = 3.1$, no correction for host galaxy

reddening was attempted. We converted magnitudes in the AB system to monochromatic fluxes following Fukugita et al. (1996) definition (see also, e.g., Tonry et al. 2012). The effective wavelength and full-width at half maximum were computed for each filter using the DES and PS1 response functions, and we find good agreement with the values reported in Tonry et al. (2012) for PS1. The modified blackbody SED corresponds to the Planck function multiplied by a linear flux suppression below the “cutoff” wavelength at 3000 Å as shown in figures A3 and A4, where the linear flux suppression corresponds to a value between zero and one, with a value of zero at zero wavelength and one at 3000 Å. A similar modified SED has been repeatedly used in the literature (see e.g., Quimby et al. 2013; Nicholl et al. 2017). Despite the fact that the linear flux suppression below 3000 Å brings the blackbody emission in better agreement with photometric and spectroscopic observations of SLSNe (see Nicholl et al. 2017), the UV-region is dominated by broad absorption lines that are far from being a perfect modified blackbody. The deviation from this modified blackbody SED is expected to be larger in the UV region than in the optical, since at optical wavelengths broad absorption lines are shallow and the continuum dominates the SN emission until a few days or weeks after maximum. Thus, the rest-frame optical and NIR emission provides a better region to fit the underlying blackbody emission. As our bolometric light curves are based on a robust determination of the blackbody parameters (T_{bb} and R_{bb}); 1) we only only objects with $z < 1.2$ in order to have at least one band, usually the *z*-band, located at a rest-frame wavelength greater than 4000 Å, where the ‘blackbody continuum’ is well defined in SLSNe and 2) for the blackbody fits only photometric bands with rest-frame effective wavelengths greater than 2800 Å are considered. To fit a modified blackbody SED a minimum of two photometric bands is sufficient, but we generally required photometry in at least three bands. Only in cases where the blackbody fits with two photometric points shows a consistent evolution with blackbody fits obtained using more bands at adjacent epochs do we keep them. We noticed that this is usually the case for fits before or close to maximum, when the SLSN emission is very similar to a blackbody and having two photometric points with wavelength greater than ~ 3500 Å can constrain very well the blackbody parameters. This is no longer true at late times, a few weeks after maximum, when the SLSN emission deviates from a blackbody and two photometric points are not able to constrain the underlying pseudo-continuum. In these cases the fits are disregarded, sometimes even using three photometric observations we obtain fits that are not good and coherent with SED fits at previous epochs, in these cases the fits are disregarded as well.

To estimate the uncertainty in the fitted blackbody parameters a similar procedure as for SN 2002gh is followed. A new set of 15, 0000 photometric observations is simulated assuming a Gaussian distribution with the standard deviation equal to the photometric uncertainty estimated using Gaussian process interpolation, and the blackbody parameters are re-computed obtaining a distribution for each of them. From the distribution obtained the uncertainties for T_{bb} and R_{bb} are estimated, computing lower and upper 1σ limits. Then, the bolometric emission using a blackbody SED with flux suppression below the “cutoff” wavelength is computed, and its corresponding 1σ uncertainty estimated.

In addition to the bolometric light curves observed luminosity (L_{obs}) light curves were constructed. To construct these light curves we summed the detected emission in the optical bands using our light curve interpolation method. When constructing these observed luminosity light curves care was put to take into account the effect of redshift in the effective wavelength and the width of the PS1 and

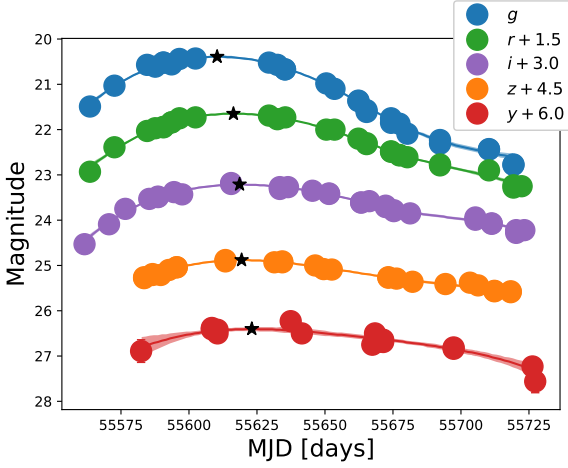


Figure A1. Gaussian process light curve interpolation for PS1-11ap. Continuous lines correspond to the light curve interpolation and shaded regions to 1σ uncertainties. Black stars mark the peak brightness for each filter.

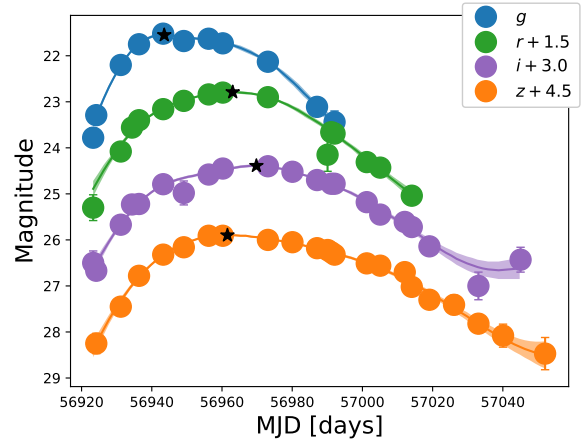


Figure A2. Gaussian process light curve interpolation for DES14X2byo. Continuous lines correspond to the light curve interpolation and shaded regions to 1σ uncertainties. Black stars mark the peak brightness for each filter.

DES filters. In tables A1 and A2 we summarize the maxima of the observed luminosity light curves.

In Fig. A5 the ratio between maximum L_{bol} and the maximum L_{obs} are presented. We find that the majority of the objects have a $L_{\text{bol}}/L_{\text{obs}}$ value between 1.5 and 3.5, with a mean value between 2.0 and 2.5. We computed the unweighted mean for $L_{\text{bol}}/L_{\text{obs}}$ for the redshift intervals $0.2 < z < 0.6$, $0.6 \leq z \leq 0.9$ and $0.9 < z < 1.21$, obtaining the following values 2.2 ± 0.4 , 2.1 ± 0.5 and 2.6 ± 0.6 , respectively. The weighted mean gives very similar values. The mean values for the PS1 sample are 2.1 ± 0.6 , 2.77 ± 0.03 and 2.6 ± 0.5 for the same redshift intervals, respectively and for the DES objects are 2.2 ± 0.2 , 1.9 ± 0.3 , and 2.6 ± 0.6 for the same intervals, respectively. We notice that the most discrepant points are the ones with larger uncertainties, and that $L_{\text{bol}}/L_{\text{obs}}$ for SN 2002gh is exactly 2.2 at $z = 0.3653$ (we do not include SN 2002gh in the computation).

Having in mind that the rest-frame wavelength and the width of the wavelength range observed in the optical bands changes dramatically over the redshift range of our sample, we assume that this heuristic relation holds beyond $z \approx 1.2$ and can be used to estimate the bolometric luminosity of PS1 and DES SLSNe with $z > 1.2$. For $z > 1.2$, we assume a $L_{\text{bol}}/L_{\text{obs}}$ ratio of 2.6, and we set the uncertainty of the $L_{\text{bol}}/L_{\text{obs}}$ ratio to 0.6. Then, we compute the L_{bol} uncertainty as $\sqrt{(0.6 \times L_{\text{obs}})^2 + (2.6 \times \sigma_{L_{\text{obs}}})^2}$.

This paper has been typeset from a $\text{\TeX}/\text{\LaTeX}$ file prepared by the author.

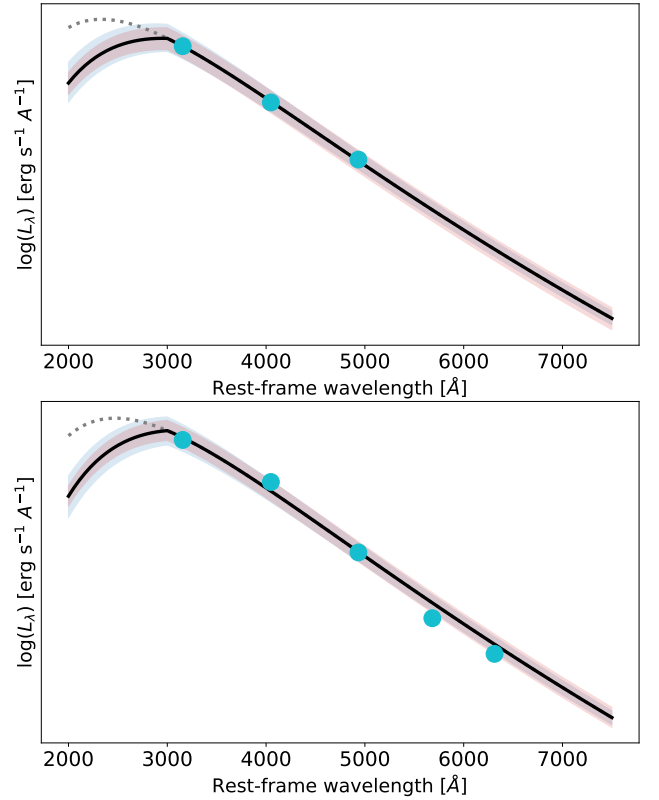


Figure A3. Blackbody fits to the interpolated photometry of PS1-11ap at -22.5 days relative to bolometric maximum (top) and at bolometric maximum (bottom). The solid line is the modified blackbody SED with a linear flux suppression below the “cutoff” wavelength at 3000 Å. The dotted line shows the full blackbody for comparison. Shaded blue regions correspond to 1 sigma uncertainty in T_{bb} (R_{bb} fixed) and shaded red regions correspond to 1 sigma uncertainty in R_{bb} (T_{bb} fixed).

Table A1. Peak bolometric and peak observed luminosities for PS1 SLSNe.

SN	MJD peak L_{bol} (days)	Peak L_{bol} ($\times 10^{44}$ erg s)	T_{bb} at peak ($\times 10^3$ K)	R_{bb} at peak ($\times 10^{15}$ cm)	MJD peak L_{obs}	Peak L_{obs} ($\times 10^{43}$ erg s)	Redshift	$E(B - V)_{gal}$
PS1-10ahf	55484.4	0.59(0.07)	$8.7^{+0.9}_{-0.7}$	$3.9^{+1.0}_{-0.8}$	55481.35	2.0(0.1)	1.10	0.0293
PS1-10awh	55497.3	2.8(0.5)	$34.8^{+10.2}_{-5.7}$	$0.8^{+0.2}_{-0.2}$	55504.8	8.1(0.2)	0.909	0.0658
PS1-10bzj	55544.9	1.4(0.3)	$28.9^{+12.2}_{-5.9}$	$0.8^{+0.2}_{-0.2}$	55559.9	4.9(0.1)	0.650	0.0068
PS1-10ky	55398.4	2.4(0.3)	$22.6^{+2.9}_{-2.2}$	$1.5^{+0.2}_{-0.2}$	55408.1	8.9(0.2)	0.956	0.0299
PS1-10pm	55334.1	1.17(0.04)	$11.2^{+0.7}_{-0.6}$	$3.4^{+0.4}_{-0.4}$	55323.6	5.9(0.2)	1.206	0.0153
PS1-11afv	–	$1.7(0.4)^{\ddagger}$	–	–	55731.4	6.6(0.4)	1.407	0.0138
PS1-11aib	55848.1	1.52(0.04)	$15.4^{+0.6}_{-0.5}$	$2.2^{+0.1}_{-0.1}$	55848.1	7.6(0.1)	0.997	0.0428
PS1-11ap	55612.6	1.42(0.03)	$11.7^{+0.3}_{-0.3}$	$3.4^{+0.1}_{-0.1}$	55612.6	8.0(0.1)	0.524	0.0059
PS1-11bam	–	$2.8(0.6)^{\ddagger}$	–	–	55889.1	10.7(0.4)	1.565	0.0234
PS1-11tt	–	$1.2(0.3)^{\ddagger}$	–	–	55710.6	4.5(0.2)	1.283	0.0080
PS1-12bmy	–	$1.3(0.3)^{\ddagger}$	–	–	56206.0	4.9(0.2)	1.572	0.0091
PS1-12bqf	56240.1	0.44(0.01)	$11.6^{+0.6}_{-0.6}$	$1.9^{+0.2}_{-0.1}$	56244.6	2.5(0.1)	0.522	0.0242
PS1-12cil	56291.1	0.9(0.1)	$19.2^{+3.4}_{-1.4}$	$1.2^{+0.1}_{-0.2}$	56303.1	2.9(0.1)	0.32	0.0234
PS1-13gt	56326.6	0.62(0.05)	$7.1^{+0.4}_{-0.3}$	$5.9^{+0.9}_{-0.8}$	56331.1	2.3(0.1)	0.884	0.0152
PS1-13or	–	$3.3(0.8)^{\ddagger}$	–	–	56393.1	12.6(0.2)	1.52	0.0308
PS1-14bj	56802.4	0.389(0.004)	$7.4^{+0.1}_{-0.1}$	$4.2^{+0.1}_{-0.1}$	56802.4	1.9(0.1)	0.5125	0.0189

Numbers in parentheses correspond to 1σ statistical uncertainties. ‡ Maximum bolometric luminosities estimated scaling the observed maximum luminosities.

Table A2. Peak bolometric and peak observed luminosities for DES SLSNe.

SN	MJD peak L_{bol} (days)	Peak L_{bol} ($\times 10^{44}$ erg s)	T_{bb} at peak ($\times 10^3$ K)	R_{bb} at peak ($\times 10^{15}$ cm)	MJD peak L_{obs}	Peak L_{obs} ($\times 10^{43}$ erg s)	Redshift	$E(B - V)_{gal}$
DES13S2cmm	56567.3	0.242(0.004)	$9.5^{+0.2}_{-0.2}$	$2.1^{+0.1}_{-0.1}$	56565.8	1.40(0.02)	0.663	0.0284
DES14C1fi	–	$1.9(0.4)^{\ddagger}$	–	–	56930.9	7.25(0.07)	1.302	0.0091
DES14C1rhg	57008.8	0.196(0.001)	$15.3^{+0.6}_{-0.5}$	$0.78^{+0.04}_{-0.04}$	57013.3	0.92(0.01)	0.481	0.0096
DES14E2slp	57041.1	0.48(0.01)	$13.1^{+0.3}_{-0.3}$	$1.61^{+0.06}_{-0.06}$	57042.6	2.58(0.04)	0.57	0.0060
DES14S2qri	–	$1.5(0.4)^{\ddagger}$	–	–	57022.7	5.9(0.2)	1.50	0.0276
DES14X2byo	56962.3	1.54(0.08)	$16.6^{+0.9}_{-0.8}$	$1.9^{+0.1}_{-0.1}$	56959.3	7.63(0.07)	0.868	0.0257
DES14X3taz	57082.6	1.28(0.06)	$11.5^{+0.9}_{-0.7}$	$3.4^{+0.5}_{-0.4}$	57082.6	7.4(0.4)	0.608	0.0220
DES15C3hav	57337.9	0.209(0.006)	$13.4^{+0.4}_{-0.3}$	$1.03^{+0.03}_{-0.03}$	57340.9	0.99(0.01)	0.392	0.0077
DES15E2mlf	–	$2.6(0.6)^{\ddagger}$	–	–	57358.0	10.2(0.4)	1.861	0.0086
DES15S1nog	57371.7	0.42(0.02)	$17.9^{+1.0}_{-0.8}$	$0.88^{+0.05}_{-0.05}$	57379.2	1.87(0.03)	0.565	0.0541
DES15S2nr	57316.8	0.441(0.005)	$10.5^{+0.1}_{-0.1}$	$2.32^{+0.04}_{-0.04}$	57321.3	2.18(0.01)	0.220	0.0293
DES15X1noe	57450.7	1.5(0.2)	$12.6^{+3.3}_{-2.0}$	$3.1^{+1.1}_{-0.9}$	57426.7	7.8(0.3)	1.188	0.0177
DES15X3hm	57239.9	1.55(0.02)	$13.9^{+0.4}_{-0.4}$	$2.6^{+0.1}_{-0.1}$	57235.4	9.46(0.09)	0.86	0.0237
DES16C2aix	57706.9	0.47(0.01)	$8.4^{+0.3}_{-0.3}$	$3.7^{+0.3}_{-0.3}$	57706.9	1.88(0.04)	1.068	0.0114
DES16C2nm	–	$1.5(0.4)^{\ddagger}$	–	–	57632.4	5.96(0.02)	1.998	0.0123
DES16C3cv	57769.9	0.264(0.003)	$6.2^{+0.1}_{-0.1}$	$5.0^{+0.1}_{-0.1}$	57673.9	1.04(0.02)	0.727	0.0103
DES16C3dmp	57723.2	0.65(0.01)	$18.8^{+0.4}_{-0.4}$	$1.00^{+0.02}_{-0.02}$	57726.2	2.76(0.02)	0.562	0.0068
DES16C3ggu	57791.6	1.7(0.7)	$29.9^{+12.7}_{-6.4}$	$0.8^{+0.2}_{-0.2}$	57800.6	4.71(0.06)	0.949	0.0074
DES17C3gyp	58152.1	1.78(0.02)	$14.9^{+1.2}_{-0.9}$	$2.5^{+0.2}_{-0.2}$	58144.6	7.3(0.2)	0.47	0.0073
DES17X1amf	58063.9	1.8(0.2)	$18.0^{+0.7}_{-0.6}$	$1.82^{+0.09}_{-0.09}$	58066.9	7.92(0.07)	0.92	0.0207
DES17X1blv	58068.2	0.273(0.006)	$10.6^{+0.4}_{-0.3}$	$1.8^{+0.2}_{-0.2}$	58068.2	1.61(0.03)	0.69	0.0213

Numbers in parentheses correspond to 1σ statistical uncertainties. \ddagger Maximum bolometric luminosities estimated scaling the observed maximum luminosities.

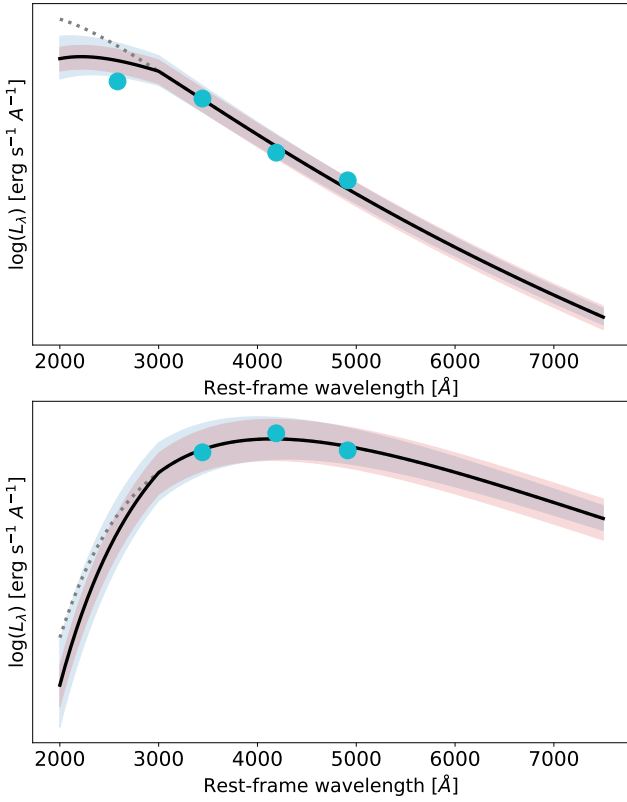


Figure A4. Blackbody fits to the interpolated photometry of DESX214byo at bolometric maximum (top) and at +22.5 relative to bolometric maximum (bottom). The solid line is the modified blackbody SED with a linear flux suppression below the “cutoff” wavelength at 3000 Å. The dotted line shows the full blackbody for comparison. Shaded blue regions correspond to 1 sigma uncertainty in T_{bb} and shaded red regions correspond to 1 sigma uncertainty in R_{bb} .

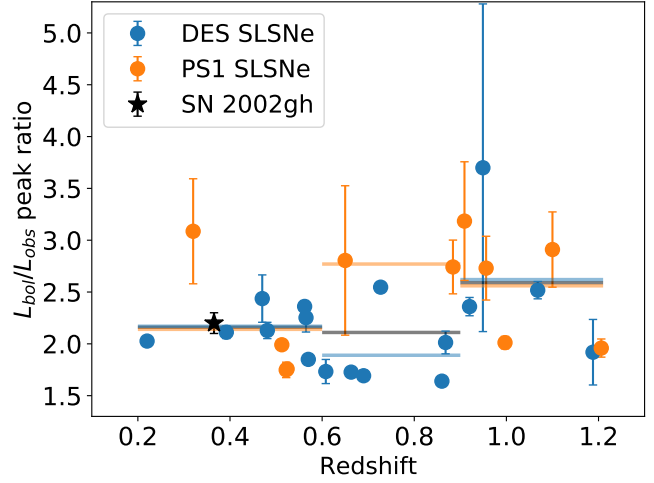


Figure A5. Ratio between the maximum bolometric luminosity and the maximum observed peak luminosity (L_{bol}/L_{obs}) as a function of redshift. We computed the unweighted mean for L_{bol}/L_{obs} for the redshift intervals $0.2 < z < 0.6$, $0.6 \leq z \leq 0.9$ and $0.9 < z < 1.21$, obtaining the following values 2.2 ± 0.4 , 2.1 ± 0.5 and 2.6 ± 0.6 , respectively. The mean for the L_{bol}/L_{obs} ratios are shown as grey horizontal lines for each redshift interval. The mean for PS1 and DES objects are shown as orange and blue horizontal lines for the same intervals, respectively. We show the location of SN 2002gh in this plot with a black star. SN 2002gh was not included in the mean computation.